Journal of
*Marine Science
and Engineering*

Article

Observation of Near-Inertial Waves Induced by Typhoon Mitag (2019) on the Southwestern East China Sea Continental Slope

Zhiling Ouyang [1,2,3], Ze Liu [1,3,4,5], Yunfei Sun [6], Bing Yang [1,2,3,4] and Yijun Hou [1,2,3,4,*]

[1] Key Laboratory of Ocean Circulation and Waves, Institute of Oceanology, Chinese Academy of Sciences, Qingdao 266071, China; ouyangzhiling@qdio.ac.cn (Z.O.); liuze@qdio.ac.cn (Z.L.); yangbing@qdio.ac.cn (B.Y.)
[2] University of Chinese Academy of Sciences, Beijing 100049, China
[3] Center for Ocean Mega-Science, Chinese Academy of Sciences, Qingdao 266071, China
[4] Laboratory for Ocean and Climate Dynamics, Qingdao National Laboratory for Marine Science and Technology, Qingdao 266237, China
[5] Qingdao Innovation and Development Base, Harbin Engineering University, Qingdao 266404, China
[6] Assets and Laboratory Management Office, Qingdao University, Qingdao 266071, China; syfcwl@qdu.edu.cn
* Correspondence: yjhou@qdio.ac.cn

Abstract: Based on horizontal velocity data recorded by a moored acoustic Doppler current profiler (ADCP) deployed on the southwestern continental slope of the East China Sea (ECS), this study investigates the characteristics of near-inertial waves (NIWs) induced by typhoon Mitag in October 2019. The results indicated that Mitag-induced near-inertial kinetic energy (NIKE) was mainly concentrated above 290 m and was subsurface-intensified; both the maximum velocity and kinetic energy of the NIWs occurred at a depth of 100 m and were 0.21 m/s and 23.01 J/m^3, respectively. The rotary vertical wavenumber spectra suggested that both downward and upward energy propagation existed. However, upward energy propagation was much smaller than downward energy propagation, mainly in the 0.007–0.014 cpm wavenumber band. The NIWs had an e-folding timescale of 9.5 days and were red-shifted as a result of the Doppler shift of the Kuroshio. Normal mode analysis suggested that the NIWs were dominated by the first and fourth baroclinic modes, which together accounted for 76.7% of the total NIKE. Spectral analysis showed that although the spectral density of the semidiurnal internal tide (M_2) peak overwhelmed that of the NIWs by a factor of approximately 30, the shear strength generated by the NIWs was comparable to that of the semidiurnal internal tide (M_2), which plays an important role in upper ocean mixing on the southwestern continental slope of the ECS. In addition, the bicoherence analysis suggested that a harmonic wave (M_2–f) was generated via the nonlinear interaction between the NIWs and semidiurnal internal tide (M_2), which reflects the energy dissipation mechanism of semidiurnal tides and NIWs on the southwestern continental slope of the ECS.

Keywords: near-inertial waves; typhoon Mitag; East China Sea; in situ observation; normal mode

Citation: Ouyang, Z.; Liu, Z.; Sun, Y.; Yang, B.; Hou, Y. Observation of Near-Inertial Waves Induced by Typhoon Mitag (2019) on the Southwestern East China Sea Continental Slope. *J. Mar. Sci. Eng.* **2022**, *10*, 202. https://doi.org/10.3390/jmse10020202

Academic Editor: Christos Stefanakos

Received: 16 December 2021
Accepted: 29 January 2022
Published: 1 February 2022

1. Introduction

Near-inertial waves (NIWs) are a type of ocean internal wave whose frequency is close to the local inertial frequency f and is generally slightly larger than the local inertial frequency f [1]. NIWs can be observed in continental shelf areas, open oceans, and closed basins, and they are ubiquitous physical phenomena in the global ocean [2–4]. NIWs play an important role in promoting ocean turbulence mixing due to the strong shear they produce [5,6]. The resulting mixing effect has a significant impact on various processes, such as the diffusion of pollutants [7], biogeochemical variability, and the energy exchange between sea and air [8,9].

Previous studies have shown that NIWs can be generated by rapidly changing strong winds [10,11] and nonlinear wave–wave interactions [12,13]. Stable or slowly evolving geostrophic currents impact seafloor topography [14,15], geostrophic adjustments in the ocean [16], mesoscale eddies [17], etc. In addition, Alford et al. [1] mentioned that NIWs could be spontaneously generated by frontogenesis and radiation by time-dependent instabilities of low-frequency flow [18,19]. NIWs are also modulated by various ocean dynamic processes, such as background flow fields and mesoscale eddies [20–25].

Among these mechanisms that generate NIWs, wind forcing is considered the most important [1]. Wind-forced NIWs are mainly caused by the rapid passage of tropical cyclones or storms. Strong winds provide kinetic energy for the mixed layer of the ocean, resulting in strong ocean currents. After several Rossby adjustment cycles, NIWs are formed, which usually show upward (downward) propagation of phase (energy) and dissipate within several days [26–28]. Studies have shown that when the translation speed of a typhoon is greater than the phase velocity of the first baroclinic mode, NIWs are generated with the typhoon track and are characterized by low order, forced baroclinic modes [29]. The oceanic response generally exhibits rightward biased features, which are attributed to the asymmetry of typhoons [30]. NIWs generated by typhoons have been investigated in several previous studies [4,11,24,31–38]. However, the NIWs excited by different typhoons usually show different characteristics in terms of intensity, frequency, and propagation direction, owing to differences in the intensities and translation speeds of typhoons, distances between typhoon centers and observation sites, and local ocean environments. Based on mooring observations, Yang et al. [11] found that the near-inertial currents induced by typhoon Hagupit were surface-intensified with a maximum of 0.52 m/s in the northern South China Sea. Hou et al. [35] examined three NIW events excited by different typhoons in the northwest Pacific and reported that the maximum of near-inertial currents varied from 0.30 to 0.58 m/s. Research by Chen et al. [23] showed that the frequency of typhoon-induced NIWs was blue-shifted due to positive background vorticity. Jeon et al. [36] revealed the poleward propagation of typhoon-induced NIWs by the Kuroshio via observations and a numerical simulation. Moreover, compared with deep water, typhoon-induced NIWs generally have a longer e-folding timescale in shallow water, showing a low-mode pattern [34].

The southwestern continental slope of the East China Sea (ECS) is located on the northeastern side of Taiwan Island and has a complex topography. Moreover, the powerful Kuroshio enters the ECS through the East Taiwan Channel, and a significant invasion of the continental shelf occurs in this sea area. In addition, typhoons generated in the western Pacific often pass through the waters near the southwestern slope of the ECS [39,40], which is conducive to the generation of NIWs. However, due to the great difficulties and high costs of in situ observations, especially under extreme weather and ocean conditions, there are few observations of NIWs generated by typhoons in this region. Fortunately, a moored array captured a significant NIW event induced by typhoon Mitag, which provided an opportunity to investigate the characteristics of the NIWs on the southwestern continental slope of the ECS. It is helpful to advance the understanding of the propagation and dissipation of NIWs in the coastal oceans, which has important theoretical and practical value for revealing coastal material diffusion and ecosystems, as well as energy transfer and local parameterization of turbulent mixing [7,9,41,42]. In addition, NIWs, as a kind of ocean internal wave, are harmful to marine projects, such as oil drilling platforms. Therefore, our study has reference significance for the implementation of offshore engineering.

2. Data and Methodology

2.1. Typhoon Mitag

Typhoon Mitag was the 18th typhoon that occurred in 2019 in the Western Pacific Ocean. The best track of Mitag was obtained from the China Meteorological Administration tropical cyclone database [43,44], which is shown in Figure 1. The temporal evolutions of the translation speeds of typhoon Mitag and distances from the typhoon center to the mooring are shown in Figure 2. On 27 September 2019, typhoon Mitag formed as a tropical depression near the Northwest Pacific (138.9° E, 13.0° N) and moved to the northwest. At 12:00 on 29 September, it strengthened from a strong tropical storm to a typhoon with a maximum wind speed of 33 m/s. It continued northwest and entered the region near Taiwan Island, and the wind speed increased further. At 15:00 on 30 September, it was the closest to the mooring, with a distance of approximately 15 km. At the same time, the translation speed and the maximum wind speed reached 8.44 m/s and 40 m/s, respectively. At 12:00 on 1 October, typhoon Mitag reached the Yangtze River estuary and turned northeast. Finally, at 12:00 on 2 October, it landed on the Korean Peninsula and was reduced to a tropical storm, which dissipated at 24:00 on 4 October.

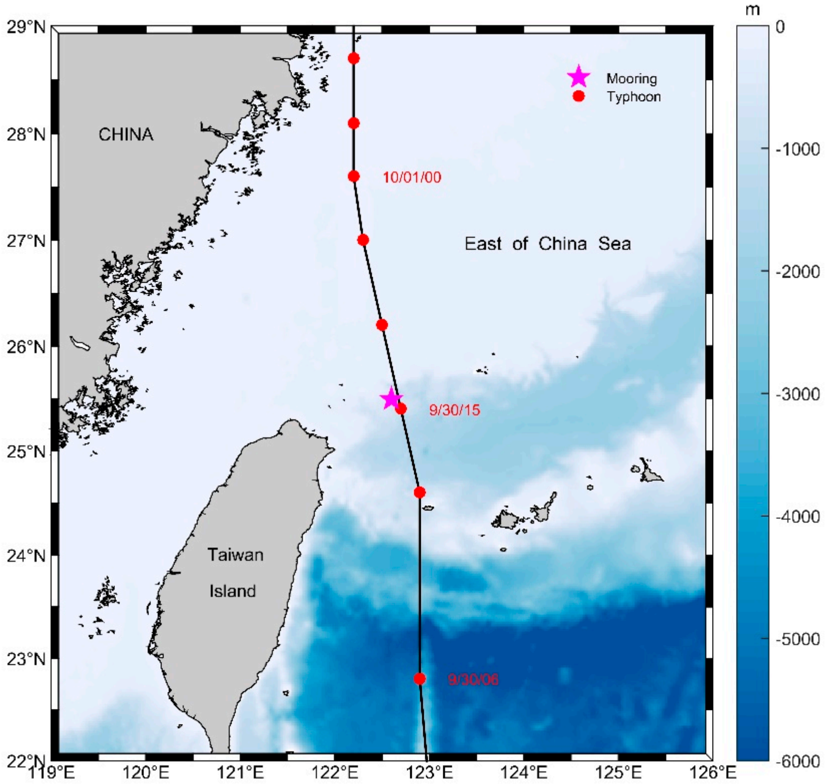

Figure 1. Bathymetry of the southern East China Sea based on ETOPO1 data. The purple star indicates mooring position. The black solid line represents the track of typhoon Mitag in 2019. Typhoon Mitag's center denoted by dots; red dots indicate intensity of typhoon Mitag, as shown in the legend.

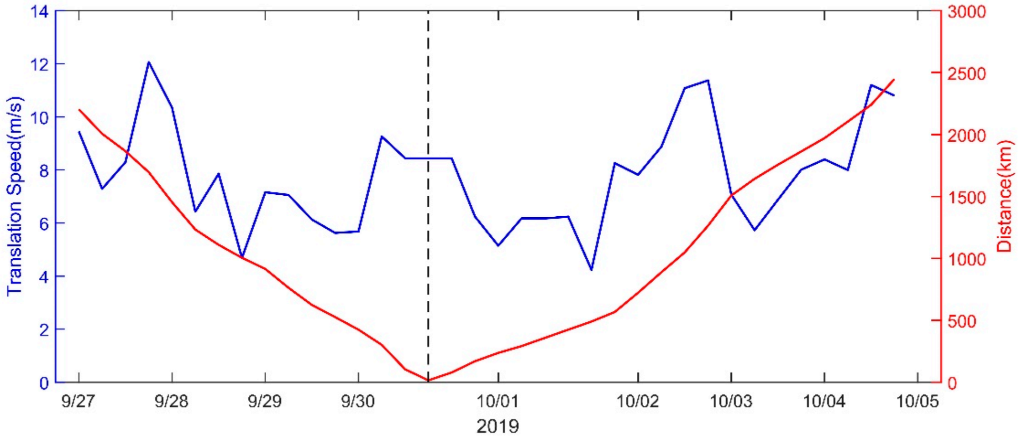

Figure 2. Translation speed (blue solid line) and distance between typhoon Mitag's center and the mooring over time from when typhoon Mitag was generated. The horizontal axis is time, left vertical axis is translation speed (m/s), and right vertical axis is distance (km).

2.2. In Situ Observations

The horizontal velocity observation data were recorded by an upward-looking 75 kHz Teledyne RDI acoustic Doppler current profiler (ADCP). The instrument was carried out on a set of submersible buoy systems that were located at 122.60° E and 25.50° N (Figure 1). The average depth of the ADCP was 561 m, and the water depth at the mooring was approximately 620 m. The observation time covered the period of the passage of typhoon Mitag. The ADCP had temporal and spatial resolutions of 0.5 h and 8 m, respectively. The ADCP observed horizontal velocity from the sea surface to 540 m; however, the data near the sea surface were contaminated by surface reflections and were discarded. Therefore, in this study, the horizontal velocity data were linearly interpolated to 50–540 m in the vertical direction every 10 m. In this study, three months of continuous meridional observed velocity data covering the entire transit period of typhoon Mitag were selected for 10-day low-pass filtering as the background currents of the Kuroshio at the mooring ($\vec{v_h}$ in Equations (11) and (12)).

2.3. Satellite Altimeter Data

The gridded satellite altimeter data used in this study integrate multiple satellites (Jason-3, Sentinel-3A, HY-2A, Saral/AltiKa, Cryosat-2, Jason-2, Jason-1, TOPEX/Poseidon, ENVISAT, GFO, and ERS1/2) with a temporal resolution of 1 d and a spatial resolution of 1/4°. Archiving, Validation, and Interpretation of Satellite Oceanographic (AVISO) data were used to provide geostrophic velocities, and sea level anomalies before and after typhoon Mitag passed the main research area. Satellite altimeter data are now released by the Copernicus Marine Environment Monitoring Service (CMEMS). The version of the datasets used in this study is "Global Ocean Gridded L4 Sea Surface Heights and Derived Variables Reprocessed (1993-ongoing)", which can be obtained from https://resources.marine.copernicus.eu/product-deail/SEALEVEL_GLO_PHY_L4_MY_008_047/DATA-ACCESS, and were accessed on 8 October 2021.

2.4. Analysis and Reanalysis Data

The buoyancy frequency of the observation period was calculated using the Global Ocean Forecasting System (GOFS) version 3.1 of the HYCOM Global Analysis dataset with a temporal resolution of 3 h, spatial resolution of 1/12°, and vertical division of 41 layers. The dataset is an operational, data-assimilative product that assimilates available satellite altimeter observations, satellite, and in situ sea surface temperatures, as well as in situ vertical temperature and salinity profiles from expendable bathythermograph (XBTs), Argo floats, and moored buoys. It has been widely used in studies on multiscale ocean phenomena off northeastern Taiwan Island [25,45,46]. The dataset is available for download from July 2014 to the present (http://www.hycom.org/data/glby0pt08/expt-93pt0, accessed on 23 July 2021). The temperature and salinity from 29 September 2019 to 15 October 2019, covering the NIW event, were selected to calculate the vertical profiles of seawater density and buoyancy frequency (later used to calculate the normal modes) at the mooring, as shown in Figure 3. Note that data on 1 October 2019 are missing.

Derived from the European Centre for Medium-Range Weather Forecasts (ECWMF), the ECWMF Reanalysis 5th Generation (ERA5) dataset was used to calculate the wind stress at 10 m over the sea surface with temporal and spatial resolutions of 1 h and 1/4°, respectively. The reanalysis wind dataset combines model data with global observations into a globally complete and consistent dataset using data assimilation. The dataset can be found here: https://www.ecmwf.int/en/forecasts/datasets/browse-reanalysis-datasets, and were accessed on 13 July 2021.

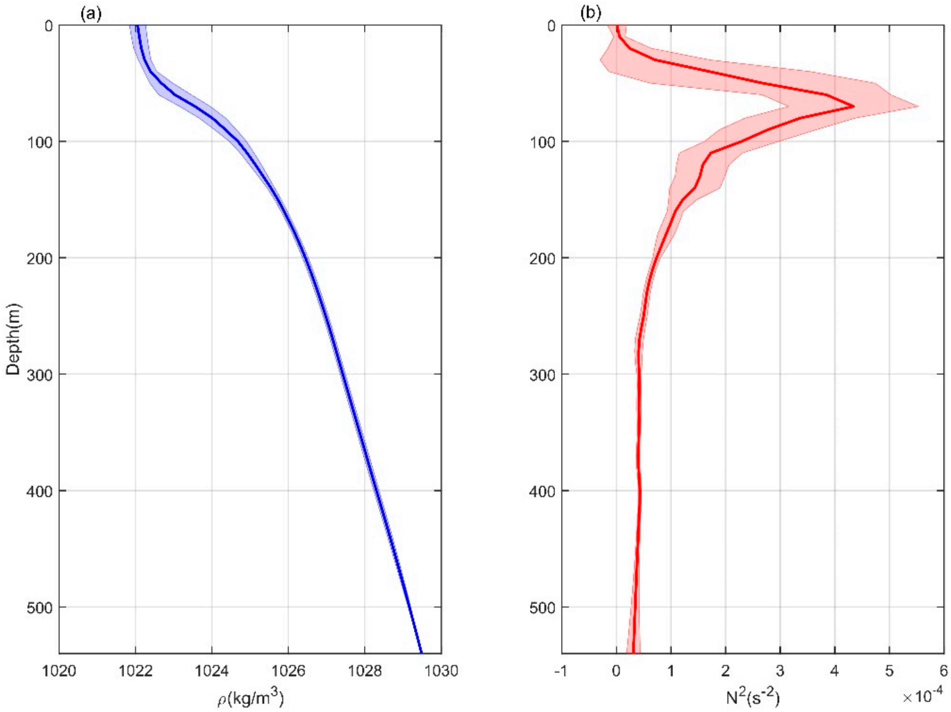

Figure 3. Vertical profiles of the time-averaged density (**a**) and buoyancy frequency squared (**b**). The light blue and red shading indicate the standard deviation in (**a**) and (**b**), respectively.

2.5. Methodology

The local inertial frequency f of the mooring is 0.0360 cph, which is similar to the frequencies of the diurnal internal tides (K_1 = 0.0418 cph, O_1 = 0.0387 cph, P_1 = 0.0416 cph, and Q_1 = 0.0372 cph). Therefore, to reduce the influence of the diurnal internal tides as much as possible, we first subtracted the diurnal internal tides (K_1, O_1, P_1, and Q_1) from the observed currents using the tidal harmonic analysis method. For convenience, the observed currents after removing the diurnal internal tides are referred to as residual currents. The rotary vertical wavenumber spectra were estimated to examine the vertical energy propagation of NIWs. First, vertical and temporal averages of the near-inertial currents were removed [47]. According to the method proposed by Leaman and Sanford [48], the near-inertial horizontal velocity can be written as $V_f(m) = u_f(m) + v_f(m)$, corresponding to the vertical wavenumber m. u_f and v_f are the zonal and meridional components of the near-inertial horizontal velocity. The Fourier transform of the near-inertial horizontal velocity V_f can be expressed as follows:

$$V_f(m) = \frac{1}{H}\int_0^H [u_f(z) + iv_f(z)]e^{-imz}dz \tag{1}$$

where H is the water depth. This transform can be divided into two parts with positive and negative wavenumbers:

$$V_f(m) = u_-(m)e^{-imz} + u_+(m)e^{imz} \tag{2}$$

where u_- and u_+ are velocity components that rotate clockwise and anticlockwise with depth, respectively. The spectra of the clockwise and anticlockwise rotating components are:

$$S_- = \frac{1}{2} < u_- u_-{}^* >, S_+ = \frac{1}{2} < u_+ u_+{}^* > \tag{3}$$

where $S_-(S_+)$ is the clockwise (anticlockwise) rotary spectrum, the angled brackets denote that the parameters within them are averaged, and the stars (*) denote the complex conjugate. $S_-(S_+)$ indicates downward (upward) propagation of energy, and the energy propagation direction is indicated by $S_{-} - S_{+}$. A positive (negative) $S_{-} - S_{+}$ indicates that the energy of NIWs propagates downward (upward).

In this study, the wind stress is calculated as follows:

$$(\tau_x, \tau_y) = \rho_a C_d \sqrt{u_{10}^2 + v_{10}^2}(u_{10}, v_{10}) \tag{4}$$

where ρ_a = 1.29 kg/m^3 is the air density, C_d is the wind stress drag coefficient, which was calculated according to the formulation recommended by Oey et al. [49], and u_{10} and v_{10} are the zonal and meridional components of the wind speed at a height of 10 m, which were obtained from the ERA5 dataset.

The modal content of the Mitag-induced NIWs was investigated in this study. The zonal and meridional components of the near-inertial currents are expressed as follows [50]:

$$\left(u_f, v_f\right) = \sum_{n=0}^{M} (u_n, v_n)\Phi_n \tag{5}$$

where $u_n(t)$ and $v_n(t)$ are the modal components of $u_f(z,t)$ and $v_f(z,t)$ with respect to mode n (n = 0, 1..., M; n = 0 for the barotropic mode and n > 0 for baroclinic modes). $\Phi_n(z)$ are the eigenfunctions of the eigenvalue problem for eigenspeed c_n:

$$\begin{cases} \frac{d^2\Phi_n}{dz^2} + \frac{N^2}{c_n^2}\Phi_n = 0 \\ \Phi_n(0) = 0, \Phi_n(-h) = 0 \end{cases} \tag{6}$$

$$\Pi_n = \rho_0 c_n^2 \frac{d\Phi_n}{dz} \tag{7}$$

where h is the water depth, and N is the buoyancy frequency. $\Pi_n(z)$ are the normal modes corresponding to velocity, and ρ_0 = 1024 kg/m^3 is the reference water density.

3. Results

3.1. Spectral Analysis

To investigate the near-inertial response of the upper ocean to typhoon Mitag, we first performed a spectral analysis of the residual current, as shown in Figure 4. A significant feature of NIWs is that the peak of their spectral density exists near the local inertial frequency f [1]. Figure 4a shows the continuous wavelet transformation of the zonal residual currents at a depth of 100 m at the mooring. Clearly, after typhoon Mitag passed the mooring, significant high-value energy appeared near the local inertial frequency f. On 2 October 2019, the energy was the highest. This indicates that the NIWs were excited by typhoon Mitag. The time evolution of the wavelet spectrum energy of the zonal residual current also shows that strong near-inertial spectrum energy existed only a few days after the passage of typhoon Mitag, while the spectral energy of the semidiurnal internal tides was almost strong during this period, reflecting the intermittent nature of NIWs, which is also an important feature to distinguish NIWs from internal tides. The depth-averaged power spectra of the zonal and meridional residual currents are shown in Figure 4b. There were significant peaks near the local inertial frequency f and the semidiurnal internal M_2 tides. However, the spectral density of the near-inertial frequency was much smaller than that of the semidiurnal internal M_2 tides, and the spectral peak of the former was approximately 1/30 of the latter. This is consistent with previous studies that showed strong semidiurnal tides in the East China Sea [51,52]. In addition, there was also a significant spectral peak at the frequency of M_2–f, which implies that nonlinear interactions between waves occur at the mooring. Note that there was no peak at the diurnal frequency, and the spectral density was very small, as shown in Figure 4. This indicates that the de-tide process using the tidal harmonic analysis method successfully reduced the interference of the diurnal signals.

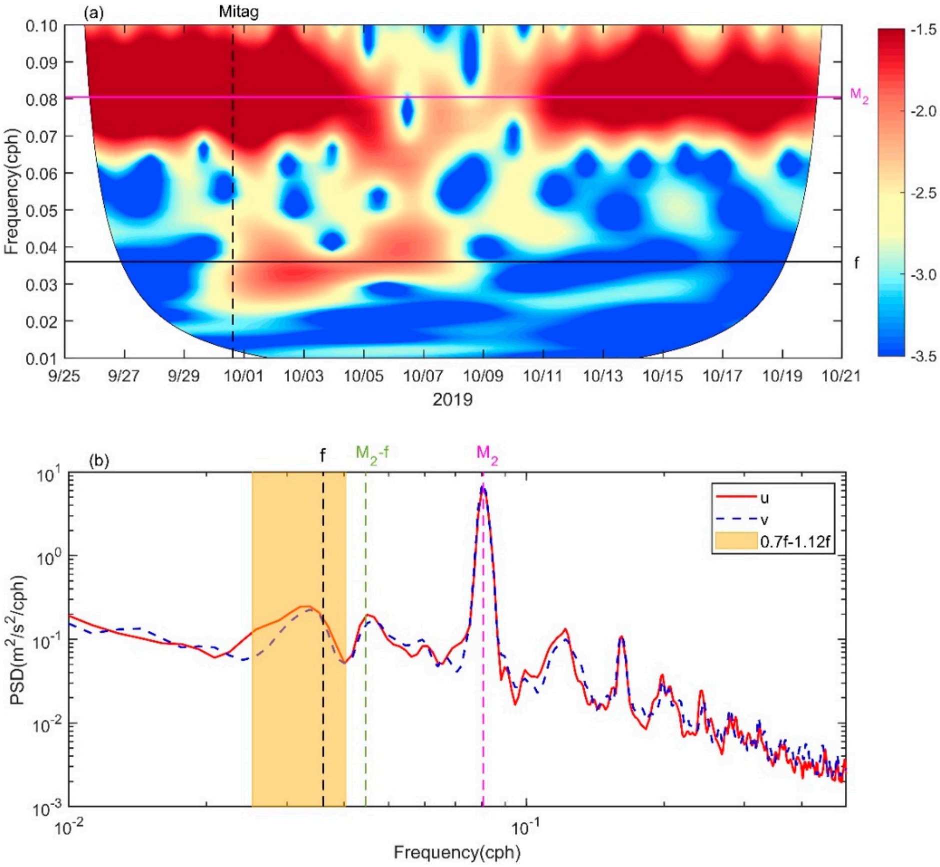

Figure 4. (**a**) Log of the magnitudes (shading) of the continuous wavelet transform of the zonal residual currents at a depth of 100 m at the mooring as a function of time and frequency. The horizontal black solid line and purple solid line indicate the local inertial frequency f and M_2 internal tides. The vertical black dashed lines denote the time when Mitag passed (15:00 on 30 September 2019). (**b**) Depth-averaged (from 50 to 540 m) power spectra of the zonal (red solid line) and meridional (blue dashed line) residual currents. The dashed lines denote the local inertial frequency f (black), the frequency of M_2–f (light green), and the frequency of M_2 internal tides (purple). The yellow shading denotes the cutoff frequency for NIWs.

3.2. Near-Inertial Currents

According to the spectral analysis results (Figure 4), with the cutoff frequency close to the troughs on both sides of the near-inertial spectrum peak as the standard, we selected the 0.70f–1.12f frequency band (yellow shading in Figure 4b) as the cutoff frequency for NIWs. A fourth-order Butterworth bandpass filter was used to extract the near-inertial currents from the residual currents. The filter was carried out twice in the forward and backward directions to eliminate all phase shifts. Figure 5 displays the vertical profiles of the zonal and meridional components of the near-inertial currents over time. NIWs usually occur a few hours after the passage of a typhoon and dissipate within a few days [53]. Figure 5 clearly shows that strong near-inertial currents were generated at the mooring after typhoon Mitag passed. The maximum zonal (meridional) near-inertial velocity was approximately 0.21 m/s (0.19 m/s) at a depth of 100 m (120 m), which is larger than that excited by typhoon Nesat observed by Yang et al. [25] (the maximum value was 0.15 m/s). The zonal velocity was slightly higher than the meridional velocity, indicating that the elliptical particle motions of NIWs have different deflection angles and sizes at different depths. The near-inertial currents showed an obvious upward propagation of the phase. According to the slope of the 0.05 m/s contour of the velocities, it takes approximately 10.50 h for the phase to propagate upward for 150 m, so the upward phase velocity was estimated to be 14.28 m/h. This value was higher than the upward phase velocities of the NIWs observed near the East China Sea continental slope by Park et al. [52] and Yang et al. [25], which were 4.68 m/h and 11.84 m/h, respectively. Near-inertial currents mainly existed above 300 m depth and presented subsurface enhancement characteristics, consistent with previous studies [23,25,35].

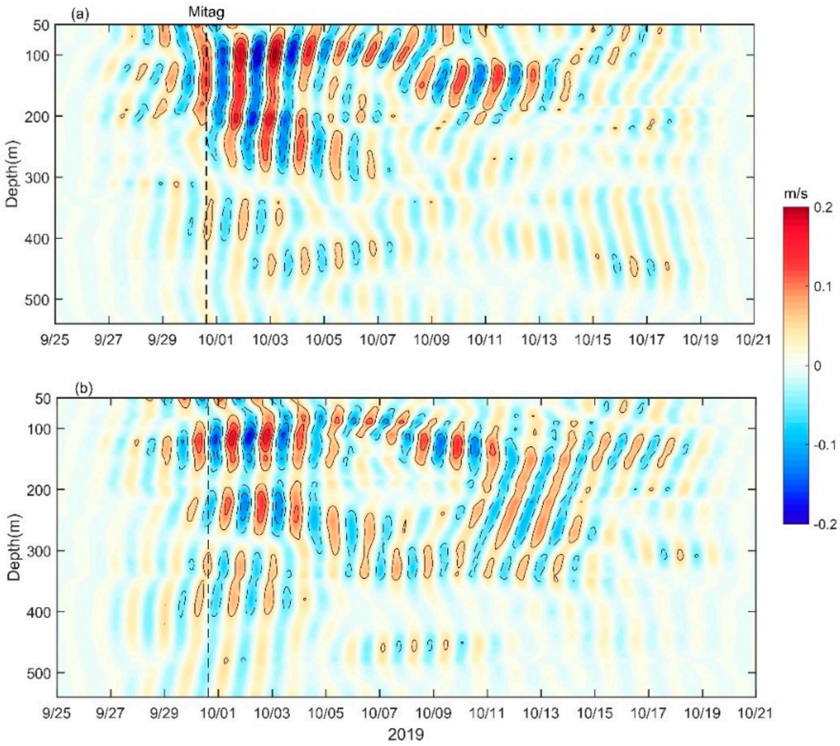

Figure 5. Vertical profiles of zonal (**a**) and meridional (**b**) near-inertial currents. Solid (dashed) contours, starting at 0.05 (−0.05) m/s, denote positive (negative) values. Intervals between adjacent contours are 0.05 m/s. Vertical black dashed lines indicate the time of closest approach to the mooring by the center of typhoon Mitag.

3.3. Near-Inertial Kinetic Energy

To analyze the characteristics of near-inertial energy produced by typhoon Mitag, we used Equation (8) to calculate the Mitag-induced near-inertial kinetic energy (NIKE).

$$NIKE = \frac{1}{2}\rho_0(u_f^2 + v_f^2) \tag{8}$$

where ρ_0 = 1024 kg/m^3 is the reference water density and u_f and v_f are the zonal and meridional near-inertial currents, respectively.

Figure 6a displays the depth–time evolutions of the NIKE. After the passage of Typhoon Mitag, the NIKE reached 290 m, based on the maximum depth of the NIKE of 5 J/m^3. There were two significant high-value kinetic energy regions, which were 70–160 m and 190–270 m. The maximum energies of the two NIKE high-value regions were 23.01 J/m^3 at 12:30 on 2 October at depths of 100 m and 17.08 J/m^3 at 9:00 on 2 October at a depth of 200 m. According to the propagation velocity of the energy core, the vertical group velocity of the NIWs was estimated to be 10.00 m/h, which is higher than the 3.60 m/h estimated by Zheng et al. [54] and the 9.71 m/h estimated by Yang et al. [11]. This result is consistent with the 10.00 m/h estimated by Yang et al. [34]. The dominant baroclinic modes of NIWs are one of the important reasons for the different vertical group velocities. High (low) baroclinic mode dominance corresponds to small (large) vertical group velocity. Therefore, the NIWs excited by typhoon Mitag were mainly dominated by the low baroclinic mode. The modal characteristics of Mitag-induced NIWs are examined later. Figure 6b shows the evolution of different depths of the low-pass filtered NIKE. The results indicate that the NIKE of the subsurface layer is stronger than that of the surface and deep layers. The NIKE at 50 m first reached its maximum value, which occurred before typhoon Mitag passed the mooring. The maximum NIKE at 120 m, 200 m, and 300 m appeared after the passage of typhoon Mitag. The time variation in the peaks of the NIKE at different depths suggests that the energy source that excited the NIWs was on the surface and that the NIKE propagated downward. It is worth noting that upward NIKE propagation occurred on approximately 5 October (Figure 6a).

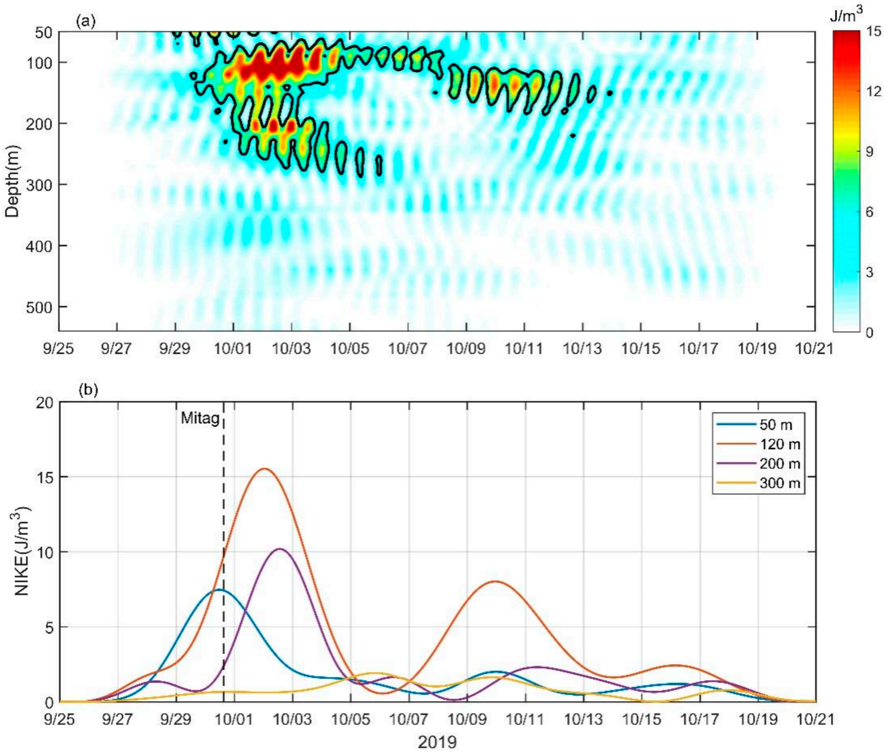

Figure 6. (**a**) Depth–time plot of near-inertial kinetic energy (NIKE) at the mooring; black contours mark the 5 J/m^3 NIKE. (**b**) Time series of one inertial period low-pass filtered NIKE at different depths; vertical black dashed line denotes the time when typhoon Mitag's center was closest to the mooring.

To further study the propagation characteristics of the NIKE, we used the rotary vertical wavenumber spectra of the near-inertial currents. Figure 7a illustrates the time evolution of the difference between the clockwise rotary spectrum (S_{-}) and the counterclockwise rotary spectrum (S_{+}). A positive value (negative value) means that energy is propagated downward (upward). It is noteworthy that the color scale of the colormap is asymmetrical, thereby highlighting the upward propagation of energy. The results show that after typhoon Mitag passed, the NIKE was dominated by downward propagation, with the smaller wavenumber band (<0.007 cpm) being the most significant. Moreover, the phenomenon of the upward propagation of energy was present, but mainly in the larger wavenumber band (0.007–0.014 cpm), which occurred from 30 September to 2 October and from 10 October to 12 October. The upward NIKE propagation in the smaller wavenumber band (0.002–0.005 cpm) on approximately 5 October corresponds to that shown in Figure 6a. The time-averaged rotary vertical wavenumber spectra show that the clockwise component is always larger than the anticlockwise component in the whole wavenumber band, especially in the wavenumber band that is less than 0.036 cpm (Figure 7b).

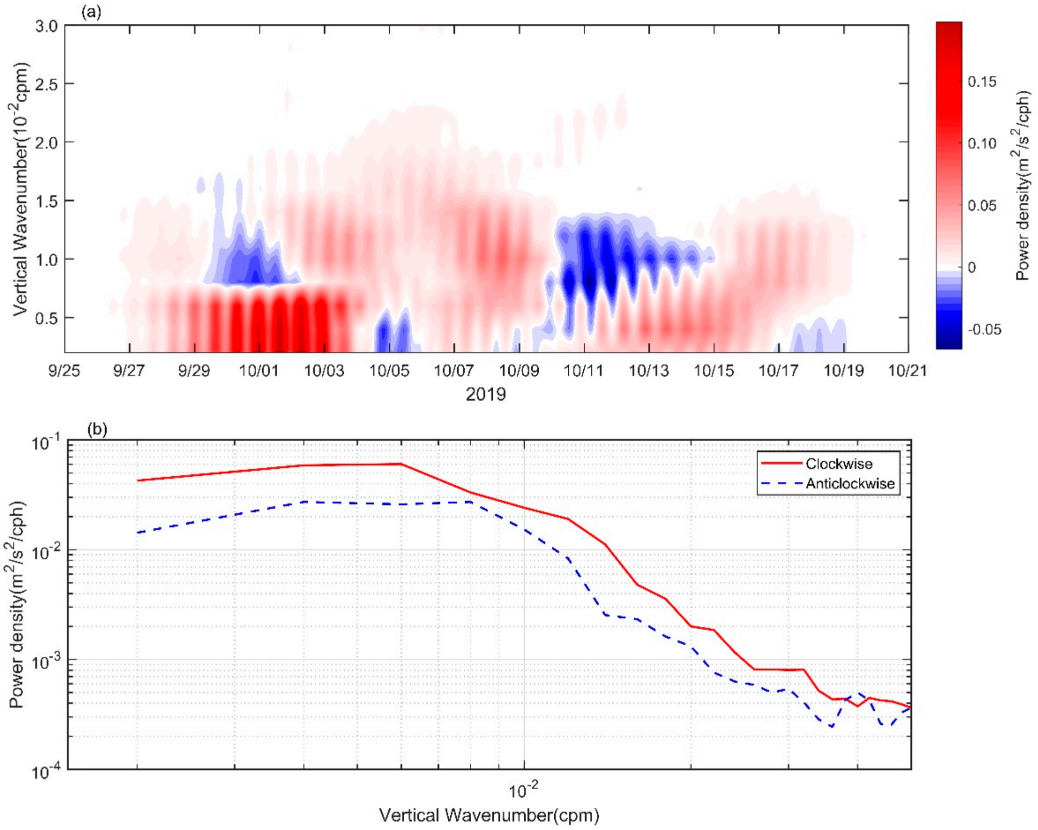

Figure 7. (**a**) Wavenumber−time map of $S_{-} - S_{+}$. (**b**) Plot of rotary vertical wavenumber spectra averaged from 25 September to 20 October 2019. The blue dashed line and red line represent anticlockwise and clockwise rotations with a depth component. cpm stands for "cycles per meter".

To investigate the damping of Mitag-induced NIWs, the e-folding time of the NIWs was estimated through the depth-averaged NIKE temporal autocorrelation function [23,25,34]. As shown in Figure 8a, the decay timescale of the NIWs was approximately 9.5 days, which was smaller than the near-inertial motion event with an e-folding time of 11 days observed by Yang et al. [25]. The longer decay timescale was determined by two consecutive wind energy inputs [25]. Figure 8b shows the time variation of 10 m wind stress on the sea surface at the mooring calculated from the ERA5 dataset, indicating that there was only one wind energy input for this near-inertial motion event. However, the decay timescale of 9.5 days is larger than the decay timescale of the NIKE in the mixed layer, which is generally less than 5 days [53]. The study of Cao et al. [38] showed that the local long decay time of the NIKE was related to the propagation of NIWs from other locations. In Figure 6a, after 6 October, significant NIKE appeared at the mooring, with a maximum value of approximately 13.24 J/m^3 occurring on 9 October. The NIKE time series at a depth of 120 m also showed that a new NIKE peak appeared on 9 October (Figure 6b). Therefore, it is reasonable to speculate that the NIWs from other locations propagate to the mooring, resulting in a longer decay timescale for this near-inertial motion event. Since the data are single-point observations, it is necessary to combine the model data to further study the three-dimensional propagation characteristics of the NIWs on the East China Sea continental slope.

3.4. Modal Content of Near-Inertial Waves

Modal content is an important characteristic of internal ocean waves [38,50]. Therefore, it is necessary to study the modal characteristics of NIWs excited by typhoon Mitag. Figure 5 shows that from 29 September to 5 October 2019 and from 6 October to 15 October 2019, the near-inertial currents had significantly different upward phase velocities of approximately

14.28 m/h and 4.56 m/h, respectively, indicating that the near-inertial currents were dominated by different modes in these two periods. The buoyancy frequency N at the mooring was calculated using HYCOM analysis data. The time evolution of the buoyancy frequency squared N^2 at the mooring is shown in Figure 9a. The results show that after typhoon Mitag passed, the depth layer with a high buoyancy frequency N was significantly lifted due to the pumping effect caused by typhoon Mitag, and the location corresponding to the maximum N became shallower. The time-averaged buoyancy frequency squared N^2 profile (Figure 3b) shows that the trend of the buoyancy frequency first increased and then decreased with depth, with a maximum value at 70 m and a maximum standard deviation.

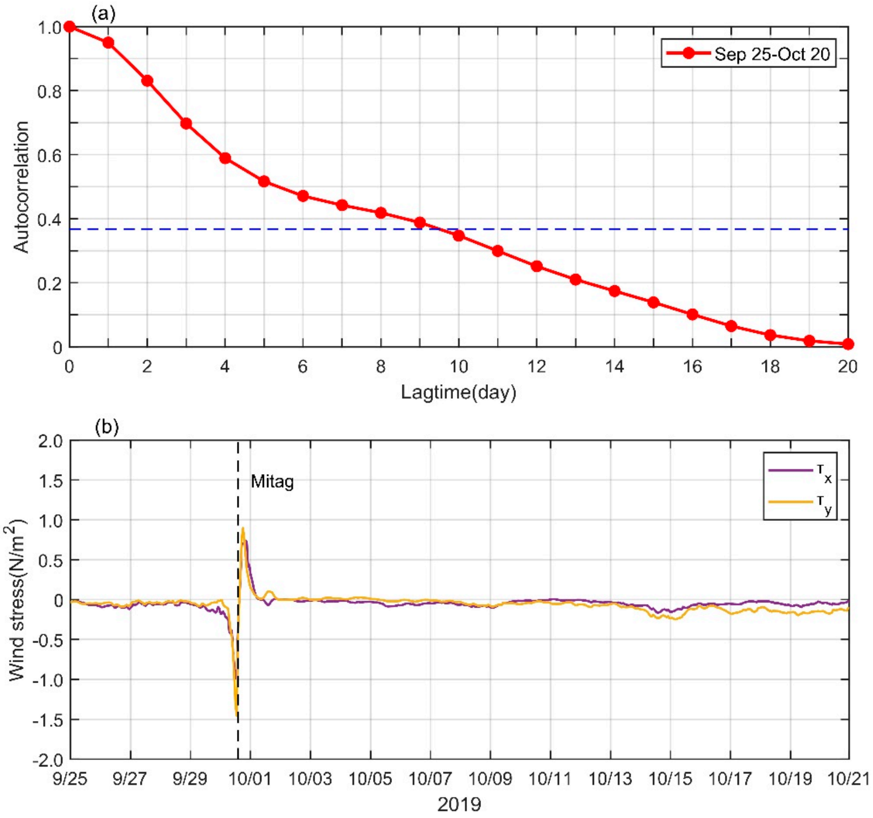

Figure 8. (**a**) Autocorrelation of the depth-averaged (from 50 to 540 m) NIKE from 25 September to 20 October 2019, and the horizontal blue dashed line denotes the value of 1/e. (**b**) Time series of the wind stress at the mooring at 10 m over the sea surface, and the purple and yellow lines represent the zonal and meridional wind stresses. The vertical black dashed line denotes the time when typhoon Mitag's center was closest to the mooring.

The mean buoyancy frequency squared N^2 from 29 September 2019 to 15 October 2019 was used to calculate the normal modes because the time-varying buoyancy frequency has little effect on the normal mode decomposition [55]. In this study, it is appropriate to use the first five baroclinic modes for modal decomposition, as shown in Figure 9b,c, which can reflect the characteristics of the NIWs to a greater extent without causing overfitting. Figure 10a,b shows the time series of the NIKE and the NIKE of the baroclinic modes, respectively. The first and fourth baroclinic modes dominated the NIKE from 29 September to 15 October, accounting for 58.0% and 18.7% of the total NIKE, respectively, and the variation in the two baroclinic modes was nearly consistent with the NIKE. The NIKE proportions of the other baroclinic modes were all less than 10%. From 29 September to 5 October, the first baroclinic mode was dominant, indicating that locally generated NIKE was dominated by the first baroclinic mode. From 6 October to 15 October, the fourth baroclinic mode was the main mode, which further indicates that the NIWs recorded by the mooring during this time period were caused by near-inertial signal propagation from other locations. This is consistent with the findings of the study of Cao et al. [38], which showed that the transmitted near-inertial signals were dominated by higher baroclinic modes.

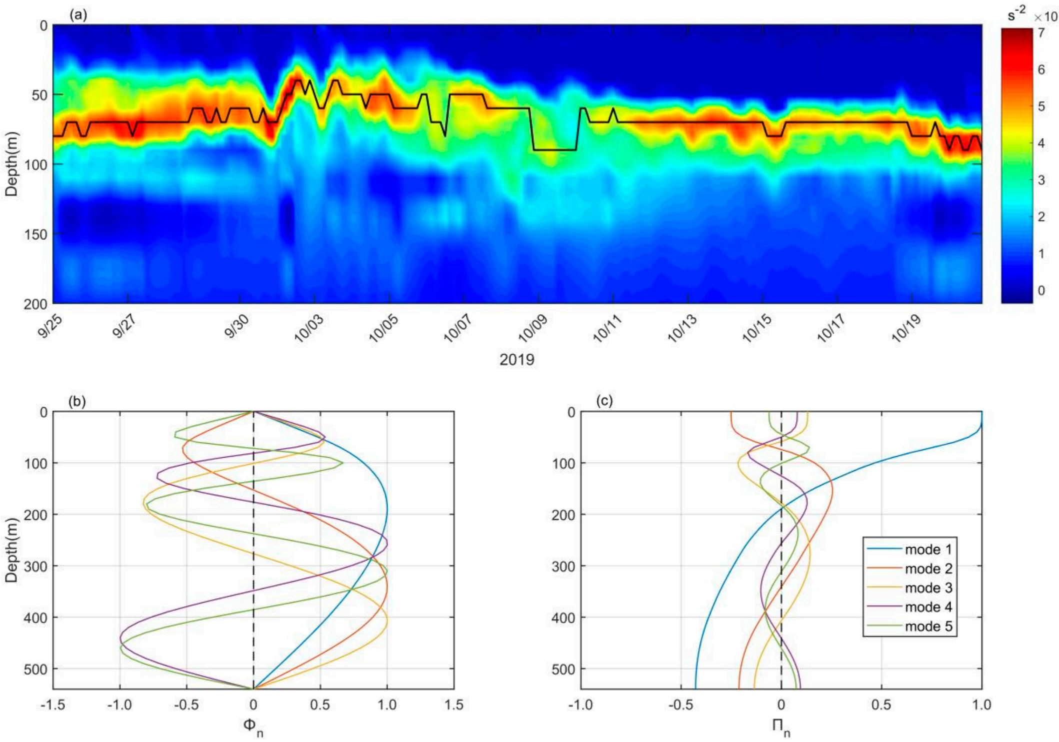

Figure 9. (**a**) Depth—time map of N^2 from 25 September to 20 October 2019 at the mooring. The black line represents the maximum N^2. Normal modes (**b**) Φ_n and (**c**) Π_n of the first five baroclinic modes at the mooring. Note that the normal modes shown in (**b**,**c**) have been normalized.

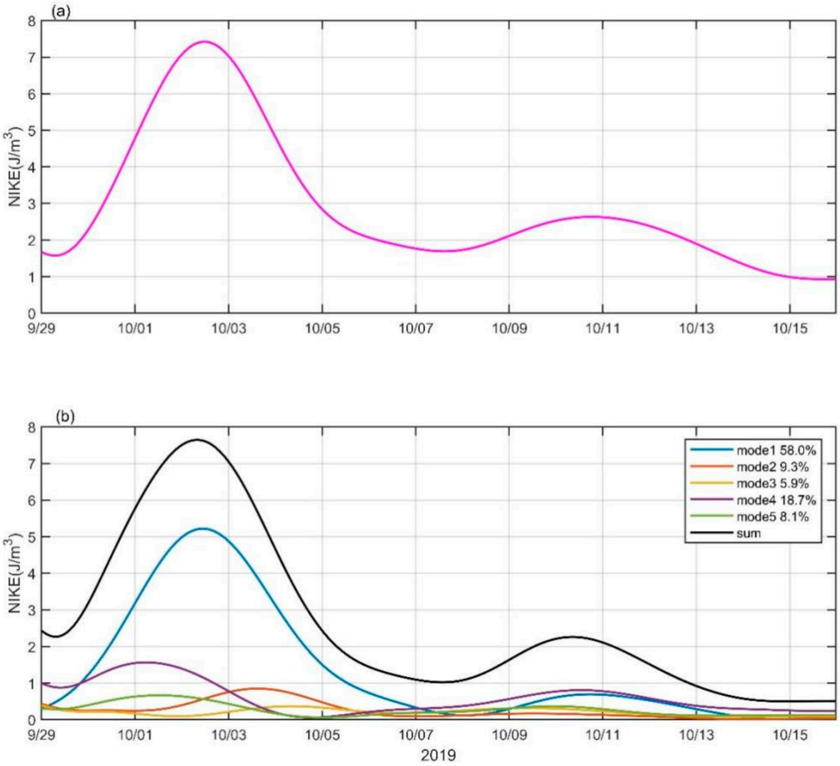

Figure 10. (**a**) Time series of one inertial period low-pass filtered NIKE averaged at depths of 50–300 m at the mooring. (**b**) Same as (**a**) but for modal NIKE, and the black line denotes the combination of these five modes.

3.5. Frequency of Near-Inertial Waves

Previous studies have shown that the frequency of NIWs is generally inconsistent with the local inertial frequency due to the influence of background vorticity and background currents [20,56,57]. Figure 11a,b shows the vertical profiles of the power spectra of zonal and meridional residual currents from 25 September to 20 October, respectively. Clearly, the high spectral density of the near-inertial frequency band 0.70f–1.12f is concentrated at depths shallower than 400 m, especially 60–160 m, which corresponds to the most significant NIKE. Figure 11c displays the near-inertial spectral peak frequencies of zonal and meridional residual currents from 50 to 400 m. The results show that the near-inertial spectral peak frequencies are basically smaller than the local inertial frequency f, showing a red-shifted characteristic. However, the near-inertial peak frequency of the zonal residual currents shows the obvious characteristic of a blue-shift from 300–330 m depth, which may be related to the background stratification [58]. The depth averages of the near-inertial peak frequencies of the zonal and meridional residual currents were 0.918f and 0.929f, respectively. In addition, the time variation in the spectral peak frequencies of the near-inertial band 0.70f–1.12f obtained by continuous wavelet transformation is shown in Figure 12. The results indicate that from 30 September to 15 October, the near-inertial spectral peak frequencies of the zonal and meridional residual currents were both smaller than the local inertial frequency f, which is consistent with the above results. The time-averaged spectral peak frequencies were 0.934f and 0.946f, respectively. However, the spectral peak frequencies increased from 4 October to 11 October. The background vorticity could modify the near-inertial frequency through the effective Coriolis frequency f_e [20] such that:

$$f_e = f + \frac{\zeta}{2} \tag{9}$$

$$\zeta = \frac{\partial v_g}{\partial x} - \frac{\partial u_g}{\partial y} \tag{10}$$

where f is the local inertial frequency, ζ is the background vorticity, and u_g and v_g are the zonal and meridional sea surface geostrophic currents, respectively. From 4 October to 11 October, a cyclonic eddy existed on the west side of the mooring, as shown in Figure 13. At the same time, the background vorticity of the mooring increased significantly (Figure 14a), resulting in an increase in the frequency of the near-inertial spectral peak (Figure 12). The average background vorticity at the mooring from 30 September to 15 October was 0.427f. Positive background vorticity generally causes the effective Coriolis frequency f_e to be greater than the local inertial frequency f, resulting in a blue-shift of the near-inertial wave frequency, but the frequency of the NIWs induced by typhoon Mitag was red-shifted. Research by Yang et al. [25] showed that the Doppler shift caused by the Kuroshio would lead to a red-shift of the NIW frequency. The mooring was affected by the background currents of the Kuroshio, as shown in Figure 13. Therefore, the Doppler shift effect caused by the Kuroshio is examined next, which can be estimated by Equations (11) and (12):

$$\begin{aligned} \omega &= \omega_0 + \vec{k} \cdot \vec{v} \\ &\approx \omega_0 + \vec{k_h} \cdot \vec{v_h} \end{aligned} \tag{11}$$

$$\vec{k_h} \cdot \vec{v_h} = \left|\vec{k_h}\right| \left|\vec{v_h}\right| \cos\alpha \tag{12}$$

where $\omega_0 \in [f, N]$ is the intrinsic frequency, ω and $\vec{k_h}$ are the Eulerian (absolute) frequency and horizontal wavenumber of NIWs, respectively.$\vec{v_h}$ is the background currents of the Kuroshio (here, it is 10-day low-pass filtered meridional raw currents at the mooring due to the northward-dominated Kuroshio, as shown in Figure 14b), and α is the angle between the horizontal phase velocity of NIWs and the horizontal background currents. For example, in the Northern Hemisphere, under the influence of northward (southward) background currents, when the NIWs propagate northward, the cosine value is positive (negative), so the Doppler shift term ($\vec{k} \cdot \vec{v}$) is greater than (less than) 0, increasing (decreasing) ω. In this study, as shown in Figure 14b, after typhoon Mitag passed, the background currents of the Kuroshio were 0.10–0.60 m/s; typical NIWs have a horizontal wavenumber of 6.28×10^{-5} m^{-1} [1,25]. The NIWs propagating southward (NIWs generated at low latitudes propagate predominantly toward the equator [59]) and the northward-dominated background currents of the Kuroshio are combined. In addition, we assume that the horizontal phase velocity of NIWs parallels the background currents of the Kuroshio. Therefore, the corresponding Doppler shift was $\vec{k_h} \cdot \vec{v_h} = -(0.10f\text{–}0.60f)$. According to Figure 14a, the effective Coriolis frequency during the period of the NIW event varied from 0.93f to 1.52f at the mooring. Hence, the above analysis shows that the Doppler shift induced by the background currents of the Kuroshio is able to cause the Mitag-induced NIWs to be red-shifted.

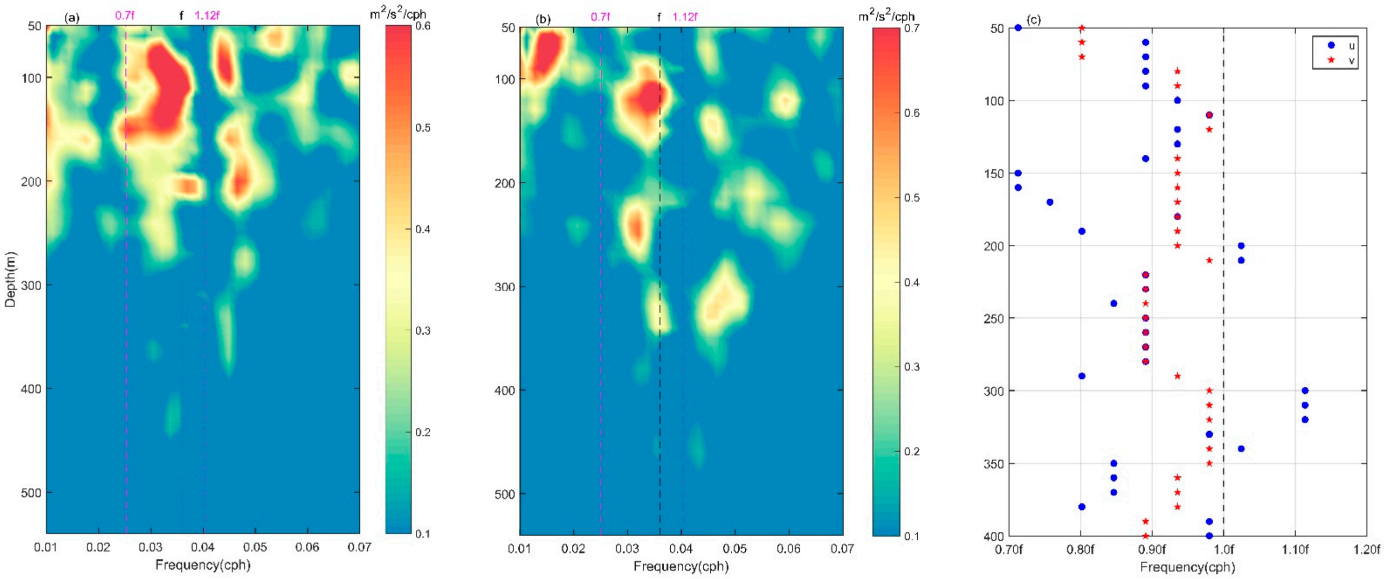

Figure 11. (**a**) Depth–frequency map of the power spectral density of zonal residual currents at the mooring. Vertical dashed lines indicate a frequency of 0.70f, local inertial frequency f, and frequency of 1.12f. (**b**) Same as (**a**), but for meridional residual currents. (**c**) Variation in the near-inertial spectral peak frequency with depth. The blue dots and red stars represent the results of the zonal and meridional residual currents, and the vertical dashed line denotes the frequency of 1.00f.

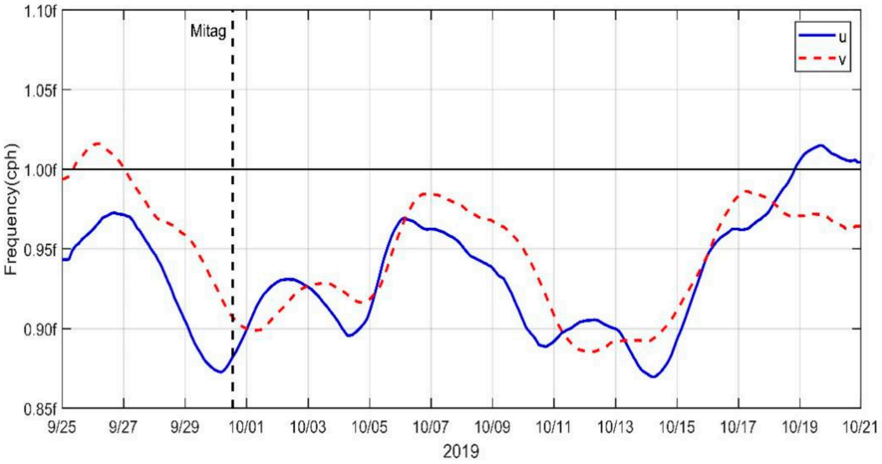

Figure 12. Time evolution of one inertial period low-pass filtered spectral peak frequency of the near-inertial band 0.70f–1.12f, and the blue solid and red dashed lines represent the zonal and meridional residual currents. The horizontal black solid line denotes the frequency of 1.00f, and the vertical black dashed line denotes the time when typhoon Mitag's center was closest to the mooring.

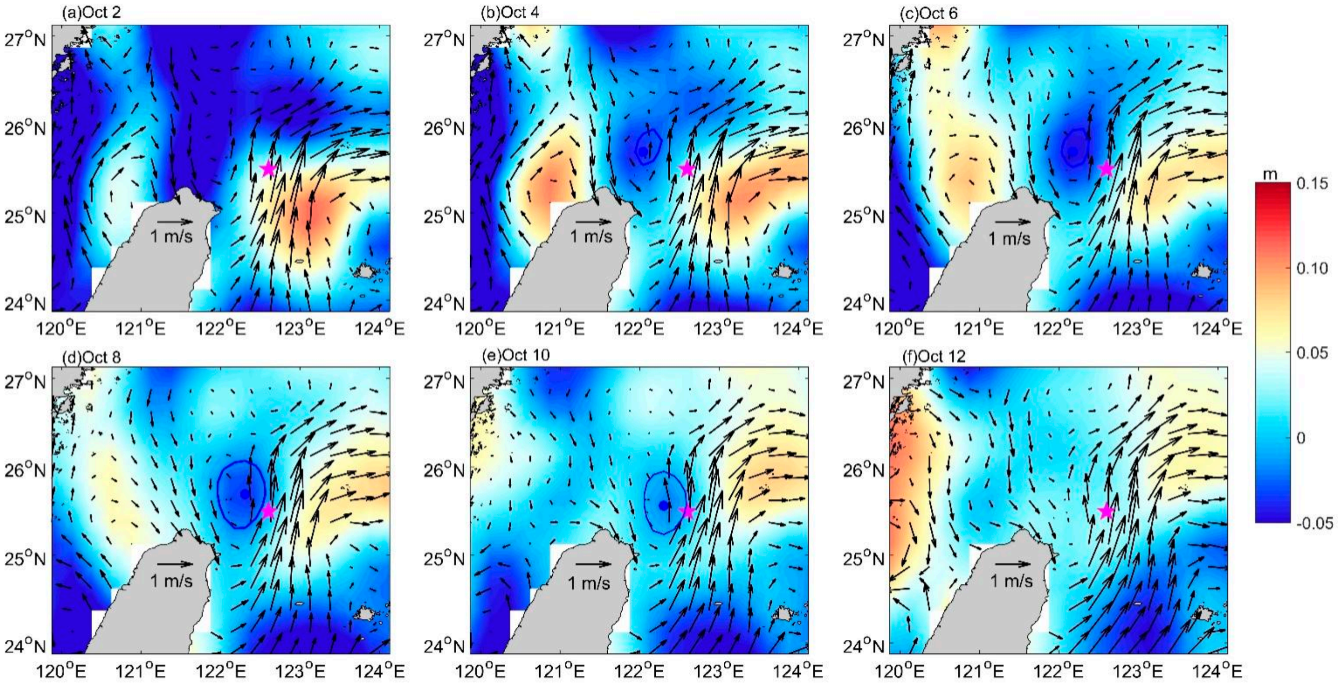

Figure 13. Distribution of sea level anomalies (colors) and geostrophic currents (arrows) in the southwestern East China Sea, and the mooring is denoted by purple star. Figures (**a**–**f**) correspond to 2 October 2019 to 12 October 2019 with an interval of 2 days. In Figures (**b**–**e**), the blue solid lines and dots represent the boundaries and centers of the cyclonic eddy, respectively, calculated according to Nencioli et al. [60].

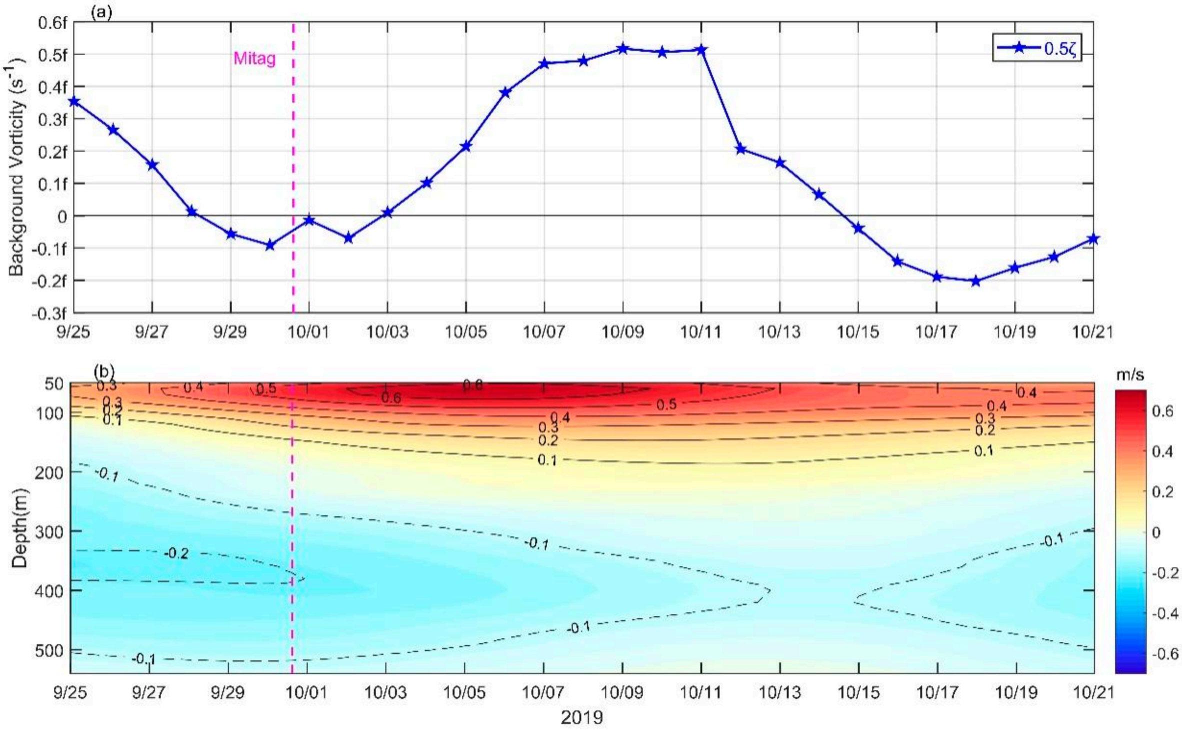

Figure 14. (**a**) Time evolution of the background vorticity at the mooring. The horizontal black solid line denotes the vorticity of zero. (**b**) Time–depth plot of 10-day low-pass filtered meridional raw currents at the mooring. Solid (dashed) contours, starting at 0.1 (−0.1) m/s, denote positive (negative) values. Intervals between adjacent contours are 0.1 m/s. In (**a**,**b**), the vertical purple dashed lines indicate the time of closest approach to the mooring by the center of typhoon Mitag.

4. Discussion

Typhoon Mitag, with a translation speed of 8.44 m/s, passed over the southwestern continental slope of the ECS on 30 September 2019. Then, we observed a significant NIW event at the mooring. Previous observations have shown that the upper ocean response to typhoons is mainly NIWs, as a result of the typhoon imparting a large momentum into the mixed layer [23,31,32,34]. Combined with the above spectral analysis, the observed NIWs were excited by typhoon Mitag. To further confirm that the NIWs were generated by the passage of Mitag and to understand how typhoons excite NIWs, we used the damped slab model, which has been widely and successfully used to explain the near-inertial currents generated in the mixed layer via wind stress [10,27,61,62]. The model is governed by the following:

$$\begin{aligned} \frac{\partial u_m}{\partial t} - f v_m &= \frac{\tau_x}{\rho_0 D} - r u_m \\ \frac{\partial v_m}{\partial t} + f u_m &= \frac{\tau_y}{\rho_0 D} - r v_m \end{aligned} \tag{13}$$

where u_m and v_m are the zonal and meridional mixed-layer currents, f is local inertial frequency, τ_x and τ_y are the zonal and meridional wind stress, ρ_0 = 1024 kg/m^3 is reference water density, D is mixed layer depth, and r is the damping coefficient. The simulated near-inertial currents were obtained by bandpass filtering of the mixed-layer currents, referring to Yang et al. [25]. The results of the slab model included Ekman currents and near-inertial currents. The wind stress was calculated by Equation (4) based on the EAR5 dataset (shown in Figure 8b). The mixed-layer depth is defined as the depth at which the temperature is 0.5 °C lower than the sea surface temperature [63] and was estimated to be 45 m from the HYCOM analysis data. The damping coefficient was set to 0.25f.

Figure 15a denotes the time evolution of the wind power input into the mixed layer calculated by the slab model at the mooring. It clearly shows that typhoon Mitag imparted much energy at the mooring as it transited. Figure 15b,c displays the zonal and meridional simulated near-inertial currents in the mixed layer and the observed near-inertial currents (here, the zonal near-inertial currents at 100 m and the meridional near-inertial currents at 120 m were chosen, with the zonal and meridional near-inertial currents being maximum at the depth) during the passage of Mitag. Although the simulated NIWs in the mixed layer were slightly larger than the observed NIWs below the mixed layer, which is the result of the decay of near-inertial energy during propagation [64,65], the simulated and observed NIWs were generally consistent. The results of the slab model and the downward (upward) energy (phase) propagation (Figures 5 and 7) verify that the observed NIWs were induced by the strong winds of Mitag. When typhoon Mitag passed through, time-varying strong wind stress was generated on the sea surface at the mooring, transferring a large amount of momentum and energy to the oceanic mixed layer and producing a resonant response in the mixed layer of water oscillating horizontally at a frequency close to the inertial frequency. After the typhoon passed, the mixed-layer near-inertial energy radiated to the thermocline and even the deep ocean in the form of NIWs [26,27,32,66]. In addition, Figure 15d indicates the time series of sea level anomalies (SLA) at the mooring. The results suggest that the time period of the cyclonic eddy affecting the mooring was from 4 October to 11 October (purple shading in Figure 15d), which lags the observed significant NIWs from September 30 (Figure 5). These results suggest that typhoon Mitag is the predominant cause of the intense NIWs that occurred on the southwestern continental slope of the ECS.

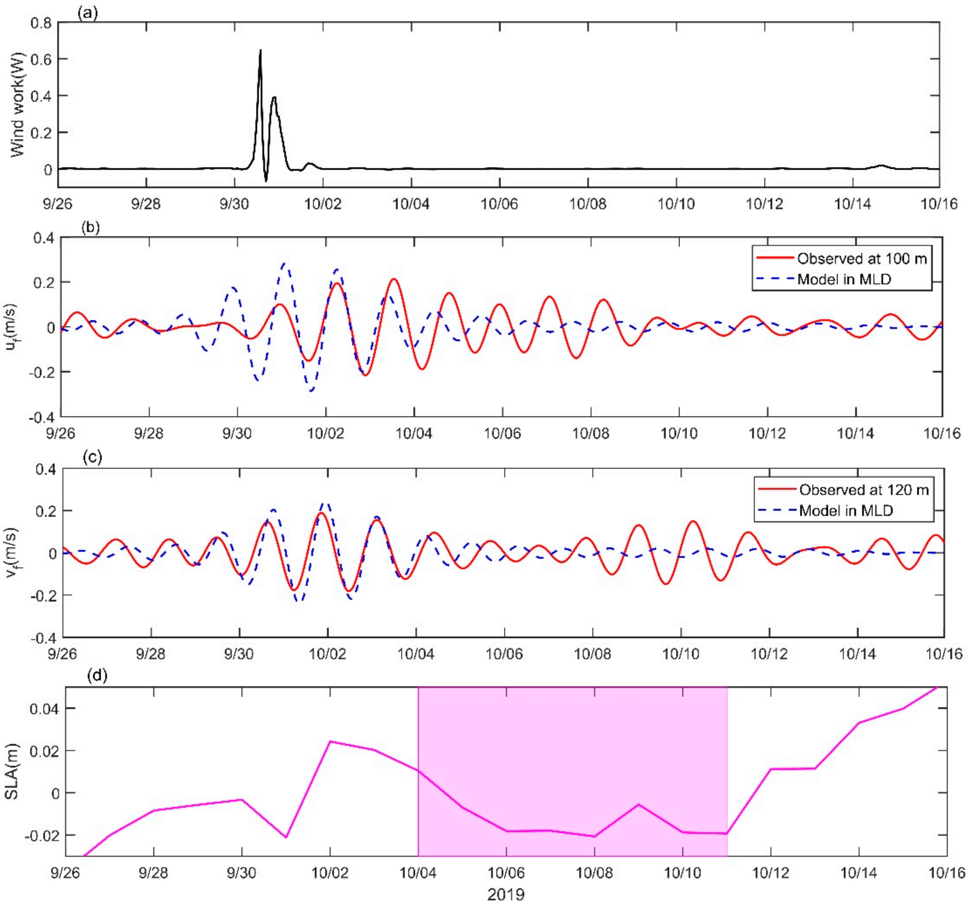

Figure 15. (**a**) The time series of the wind work computed from the slab model. (**b**) Comparison of the zonal near-inertial currents of observation (solid red line) below the mixed layer and simulation (dashed blue line) in the mixed layer, with (**c**) the same as (**b**), but for the meridional near-inertial currents. (**d**) The time evolution of the sea level anomalies at the mooring, and the purple shading indicates the period when the cyclonic eddy affected the mooring.

Energetic M_2 barotropic-to-baroclinic conversion occurs in the ECS [67,68]. The above spectral analysis shows that even the significant near-inertial internal waves were generated by the typhoon, the spectral density of which was much smaller than that of M_2 internal tide. Both internal tides and NIWs have important contributions to ocean mixing [69,70]. The shear values of currents can represent the strength of seawater mixing and the energy dissipation rate. Larger shear values indicate that the stronger the mixing is, the greater the energy dissipation rate. To study and compare the mixing effect caused by the Mitag-induced NIWs and the M_2 internal tide on the continental slope of the ECS, the vertical shear spectra of the residual currents were calculated. The depth-averaged vertical shear spectra of zonal and meridional residual currents are shown in Figure 16. The results show that there is strong shear at near-inertial and semidiurnal frequencies, and the strengths of both are equal. Therefore, although the NIWs excited by typhoon Mitag have much less energy than the M_2 internal tide, the ocean mixing caused by the NIWs was comparable to that of the strong M_2 internal tide. To further study the shear characteristics of the NIWs and M_2 internal tide, the shear is calculated as follows:

$$s = \sqrt{\left(\frac{\partial u_b}{\partial z}\right)^2 + \left(\frac{\partial v_b}{\partial z}\right)^2} \tag{14}$$

where u_b and v_b are the zonal and meridional components of the NIWs or M_2 internal tide, respectively. According to the spectral analysis results (Figure 4b), the frequency band of

(0.0705–0.0881) cph corresponding to 1.96f–2.45f was selected as the cutoff frequency for extracting M_2 internal tides. Figure 17a,b displays the depth–time plots of 24 h low-pass filtered shear caused by the NIWs and M_2 internal tide, respectively. Clearly, the strong shear generated by the NIWs and M_2 internal tide mainly occurred above 120 m, and the maximum shear values were 0.0117 s^{-1} and 0.0182 s^{-1}, corresponding to the former and the latter, respectively. Strong near-inertial shear corresponds to weak near-inertial currents (Figures 5 and 6a), while strong M_2 internal tidal shear is consistent with strong M_2 internal tide. In addition, compared with near-inertial shear, M_2 internal tidal shear was also significant below 300 m.

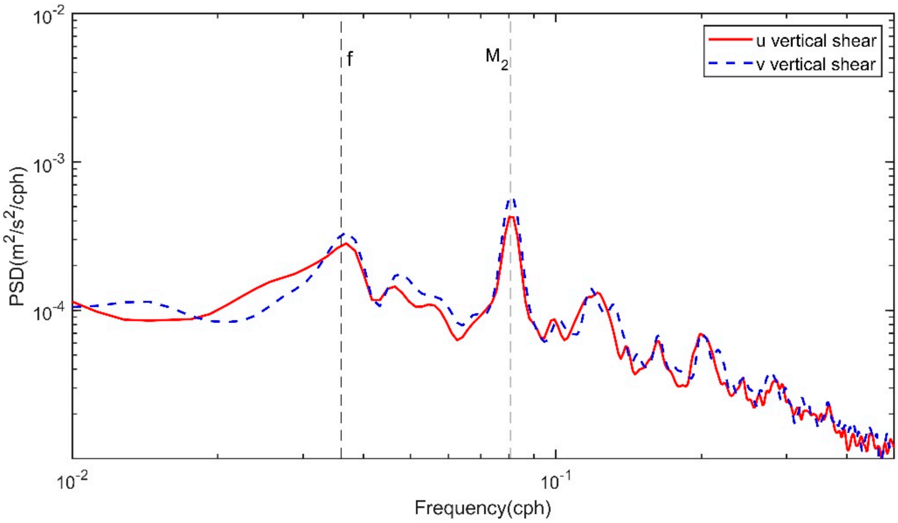

Figure 16. Depth-averaged (from 50 to 540 m) power spectra of the shear of zonal (red solid line) and meridional (blue dashed line) residual currents. The black dashed lines denote the local inertial frequency f and the frequency of the M_2 internal tide.

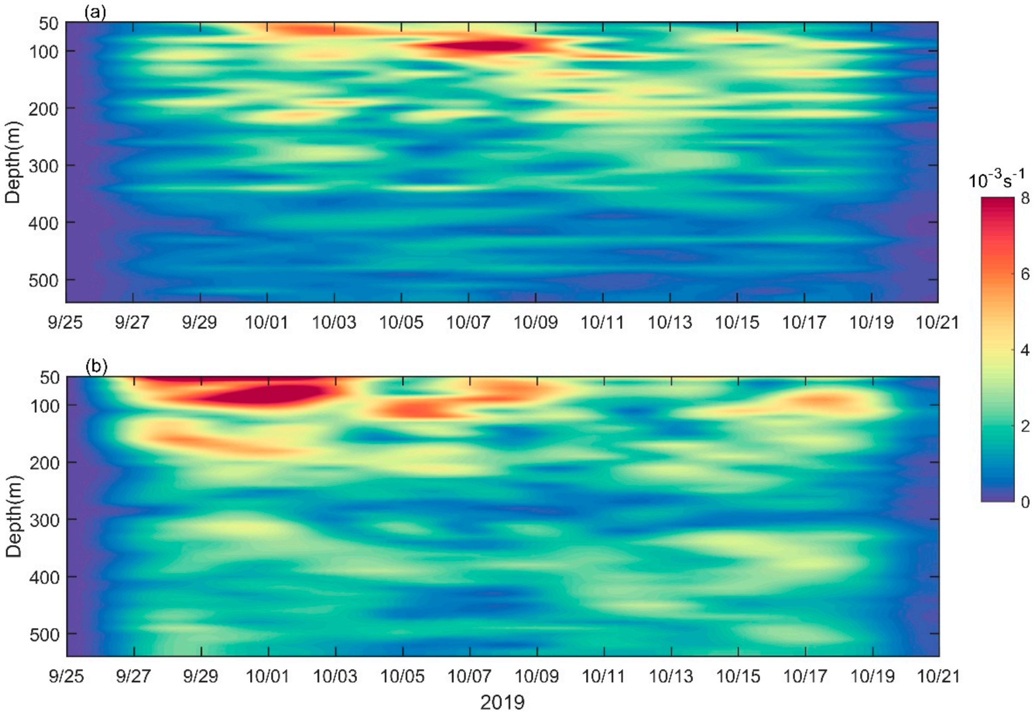

Figure 17. Depth−time maps of the low-pass filtered vertical shear of the (**a**) NIWs and (**b**) M_2 internal tide.

Spectral analysis results show that there was a spectral peak at the frequency of M_2-f (Figure 4b). It is speculated that M_2-f waves were generated by the nonlinear wave–wave interactions between the NIWs and M_2 internal tides. Because the two-wave coupling theory indicates that the two main waves are coupled into the third wave, the frequency relationship between them satisfies $w_1 \pm w_2 = w_3$, and the wavenumber relationship satisfies $k_1 \pm k_2 = k_3$ [71]. To estimate the occurrence of the nonlinear interaction process between internal waves, the bicoherence of the residual currents, which is the normalized version of the bispectrum, was calculated. This method can effectively estimate the phase-locking between waves with different frequencies. It has been widely used to distinguish between nonlinearly coupled waves and independent waves [12,13,72–76]. The bispectrum is expressed in the frequency domain as:

$$\begin{aligned} B(\omega_1,\omega_2) &= E\left[X_{\omega_1} Y_{\omega_2} Z^*_{\omega_1+\omega_2}\right] \\ &= E\left[|X_{\omega_1}||Y_{\omega_2}||Z_{\omega_1+\omega_2}|e^{-i(\theta_1+\theta_2+\theta_3)}\right] \end{aligned} \tag{15}$$

where $E[]$ is the expected value; * denotes the conjugate; X_ω, Y_ω, and Z_ω are the Fourier coefficients of variables x, y, and z in frequency space. θ_1, θ_2, and θ_3 are the relative phases of the respective Fourier coefficients. The bicoherence can be expressed as follows:

$$b^2(\omega_1,\omega_2) = \frac{|B(\omega_1,\omega_2)|^2}{E\left[|X_{\omega_1}|^2\right] E\left[|Y_{\omega_2}|^2\right] E\left[|Z_{\omega_1+\omega_2}|^2\right]} \tag{16}$$

With the influence of the wave amplitude eliminated, bicoherence measures the phase-locking between the interacting triads.

Figure 18a gives the bicoherence values with depth for the frequency bins [f, M_2-f] and [f, M_2], which were calculated from the zonal residual currents. In the thinner depth layer near a depth of 130 m, the bicoherence values around the [f, M_2-f] and [f, M_2] frequencies exceed the 90% confidence interval or even the 95% confidence interval. At the same time, the bicoherence analysis at 130 m shows that significant bicoherence values occurred around the [f, M_2–f] and [f, M_2] frequencies (Figure 18b). Figure 19 shows the depth-averaged kinetic energy in the near-inertial, M_2 (0.0705–0.0881 cph) and M_2–f (0.0417–0.0543 cph) frequency bands at the mooring. Significant M_2–f kinetic energy occurred during the period when the kinetic energy of M_2 and near-inertial kinetics were both strong. The linear correlation coefficient between the near-inertial and M_2–f kinetic energy was 0.94 ($p < 0.01$). Through ideal experiments and simple derivation, Cao et al. [75] pointed out that when NIWs have a nonlinear interaction with M_2 internal tides, they have a significant bicoherence value around the frequencies of [f, M_2–f] and [f, M_2]. Therefore, this evidence indicates that M_2–f waves are the result of the nonlinear interaction of the NIWs and M_2, and the energy transfers from M_2 and f to M_2–f, reflecting a mechanism of energy dissipation of NIWs and semidiurnal internal waves.

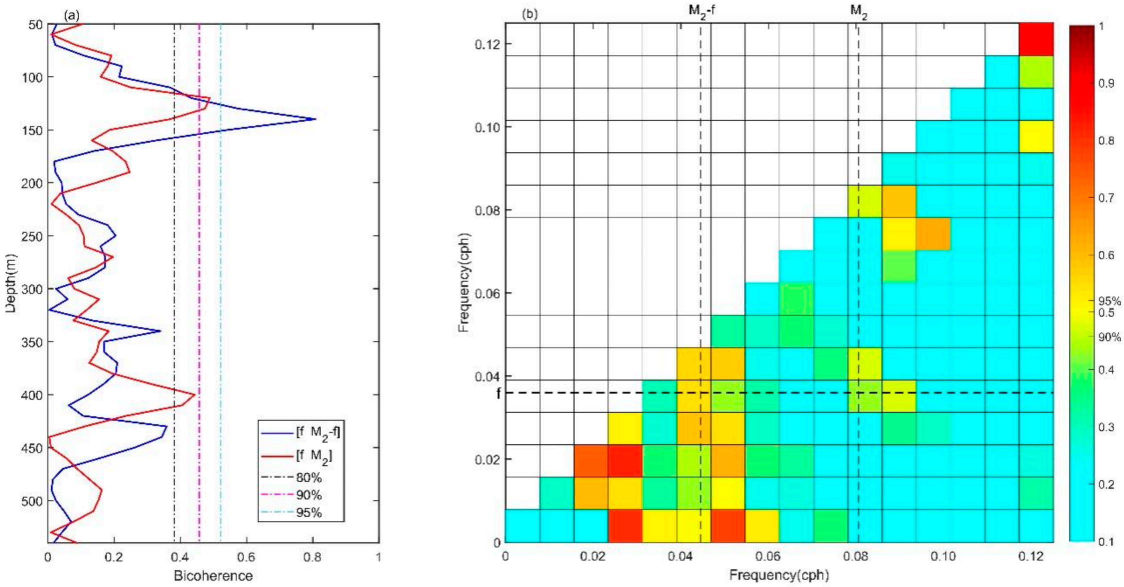

Figure 18. (**a**) Bicoherence values between near-inertial frequency *f* and M_2–*f* (blue line) and M_2 (red line) frequency zonal residual currents plotted as a function of depth. Three vertical dashed lines denote the 80% (black), 90% (purple), and 95% (light blue) confidence intervals. (**b**) Bicoherence values of zonal residual currents at a depth of 130 m. The 90% and 95% confidence intervals are marked in the color bar.

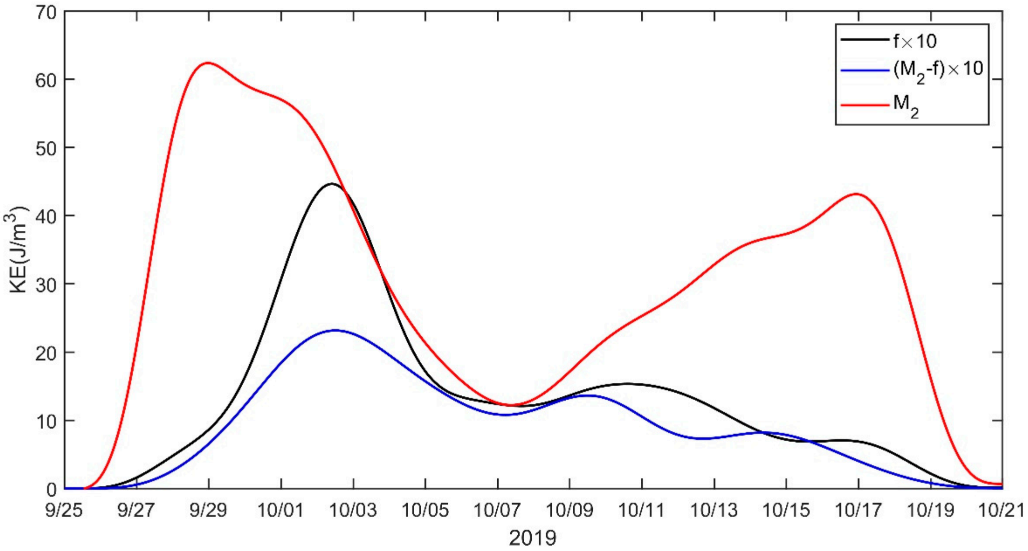

Figure 19. Twenty-four-hour low-pass filtered depth-averaged kinetic energy in the near-inertial (black), M_2–*f* (blue), and M_2 (red) frequency bands. Note that the kinetic energy in the *f* and M_2–*f* frequency bands is amplified by a factor of 10, referring to Cao et al. [75].

5. Conclusions

On 30 September 2019, typhoon Mitag passed over the southwestern continental slope of the ECS, generating strong NIWs, which were fully captured by an ADCP deployed here. Based on in situ observations as well as analysis and satellite data, the horizontal velocity, energy, modal, and frequency characteristics of the NIWs are analyzed.

Analysis of the power spectra and continuous wavelet spectra shows that a significant spectral density appeared near the local inertial frequency *f* after the passage of typhoon Mitag, but the near-inertial spectral density peak was approximately 1/30 of that of semidiurnal internal M_2 tides. This value indicates that the high-frequency movement on the southwestern continental slope of the ECS was dominated by semidiurnal internal tides. The vertical shear spectra show that the shear spectrum energy of the near-inertial band is equivalent to that of semidiurnal internal M_2 tides, indicating that the NIWs had much less energy than semidiurnal internal M_2 tides, but the strong shear generated by the NIWs resulted in turbulent ocean mixing comparable to that of semidiurnal internal M_2 tides. In addition, spectral analysis shows that there was also a significant spectral peak at the frequency of M_2–f. The simultaneous enhancement of near-inertial currents and M_2–f currents as well as the significant bicoherence values of the [f, M_2–f] frequency indicate that this was the result of nonlinear interaction between the NIWs and M_2–f waves, which reflects a mechanism of energy dissipation of internal tides and NIWs. Moreover, Yang et al. [76] showed that the M_2 internal tide transmits energy on a smaller scale through the parametric subharmonic instability (PSI) mechanism, revealing a complex mechanism of energy dissipation of internal tides and NIWs on the southwestern continental slope of the ECS. It is also necessary to further study the contribution of ocean mixing caused by NIWs compared with internal tides.

The time–depth profile of the near-inertial currents shows that the maximum zonal (meridional) Mitag-induced near-inertial currents with a velocity of 0.21 m/s (0.19 m/s) occurred at a depth of 100 m (120 m). The zonal velocity is slightly greater than the meridional velocity, showing the motion characteristics of elliptical particles of NIWs. Based on the slope of the 0.05 m/s velocity contour, the upward phase velocity was estimated to be 14.28 m/h. The NIKE was mainly shallower than 290 m, two high-value areas of kinetic energy showed subsurface enhancement characteristics, and the maximum kinetic energy was 23.01 J/m^3. According to the propagation velocity of the energy core, the vertical group velocity of the NIWs was estimated to be 10.00 m/h. The time variation in the NIKE at different depths showed that the NIKE of 50 m reached its maximum value before the center of typhoon Mitag passed the mooring, while the NIKE values of 120 m, 200 m, and 300 m reached their maximums after the center of typhoon Mitag passed the mooring. As the depth increases, the time delay to reach the maximum value indicates that the NIKE excited by typhoon Mitag propagated downward. The time-averaged rotary vertical wavenumber spectra showed that the NIKE propagates significantly downward in the wavenumber band (<0.036 cpm). The time variation in the rotary vertical wavenumber spectra shows that there was also a weak upward NIKE propagation phenomenon, mainly in the 0.007–0.014 cpm wavenumber band, and it occurred in different time periods. The time autocorrelation function of the deep-averaged NIKE shows that the e-folding time of the NIWs was 9.5 days; this value is larger than the decaying timescale of the NIKE in the mixed layer, which was generally less than 5 days [53]. The longer decaying time scale of the NIKE may be related to the propagation of near-inertial signals excited by typhoon Mitag at locations other than the mooring.

Normal mode analysis shows that the NIWs were dominated by the first baroclinic mode, followed by the fourth baroclinic mode. These two baroclinic modes account for 58.0% and 18.7% of the total NIKE, respectively. However, the NIKE of the first baroclinic mode was dominant from 29 September to 5 October, and the NIKE of the fourth baroclinic mode was dominant from 6 October to 15 October. The former corresponded to a large upward phase speed (14.28 m/h), and the latter corresponded to a small upward phase speed (4.56 m/h). The frequencies of the zonal and meridional near-inertial currents were 0.918f and 0.929f, respectively. Although the average background vorticity was 0.427f, the NIWs excited by typhoon Mitag exhibited a red-shift due to the Doppler shift effect of the Kuroshio. Interestingly, from 4 October to 11 October, affected by a cyclonic eddy, the positive background vorticity at the mooring increased significantly, but the frequency of the NIWs was still lower than the local inertial frequency f. This implies that the frequency of NIWs in the Kuroshio area of the ECS is mainly affected by the Kuroshio Doppler shift effect. Further research is needed to provide more evidence.

Author Contributions: Conceptualization, Y.H.; methodology, Z.O. and B.Y.; formal analysis, Z.O. and Y.S.; writing—original draft preparation, Z.O.; writing—review and editing, Z.O., Z.L., and Y.S.; supervision, Z.L. and Y.S.; funding acquisition, Y.H. and Z.L. All authors have read and agreed to the published version of the manuscript.

Funding: The research was funded by the National Natural Science Foundation of China, grant numbers 41630967, 41776020, and 42076002.

Institutional Review Board Statement: Not applicable.

Informed Consent Statement: Not applicable.

Data Availability Statement: Data are available in a publicly accessible repository that does not issue DOIs. The best track data of typhoons were from the China Meteorological Administration tropical cyclone database (CMA, https://tcdata.typhoon.org.cn/zjljsjj_zlhq.html, accessed on 7 June 2021). The satellite altimeter data were obtained from the Copernicus Marine Environment Monitoring Service (CMEMS, https://resources.marine.copernicus.eu/product-deail/SEALEVEL_GLO_PHY_L4_MY_008_047/DATA-ACCESS, accessed on 8 October 2021). The ERA5 wind products were obtained from the European Centre for Medium-Range Weather Forecasts (ECWMF, https://www.ecmwf.int/en/forecasts/datasets/browse-reanalysis-datasets, accessed on 13 July 2021). The HYCOM+NCODA Global Analysis data are available at https://www.hycom.org/data/glby0pt08/expt-93pt0, and were accessed on 23 July 2021. The ETOPO1 Global Relief Model was downloaded from https://www.ngdc.noaa.gov/mgg/global/global.html, and was accessed on 16 June 2020.

Acknowledgments: The acquisition of mooring data was supported by the NSFC Open Research Cruise China (Cruises No. NORC2020-02), funded by the Ship-time Sharing Project of NSFC, China. This cruise was conducted onboard R/V "Xiang Yang Hong 18" by the First Institute of Oceanography, State Oceanic Administration, China. We also thank the associate editor and the anonymous reviewers for their useful feedback that improved this paper. The research was funded by the National Natural Science Foundation of China, grant numbers 41630967, 41776020, and 42076002. The ERA5 wind products were from the European Centre for Medium-Range Weather Forecasts (ECWMF, https://www.ecmwf.int/en/forecasts/datasets/browse-reanalysis-datasets, accessed on 13 July 2021).

Conflicts of Interest: The authors declare no conflict of interest.

References

1. Alford, M.H.; MacKinnon, J.A.; Simmons, H.L.; Nash, J.D. Near-Inertial Internal Gravity Waves in the Ocean. *Annu. Rev. Mar. Sci.* **2016**, *8*, 95–123. [CrossRef] [PubMed]
2. Millot, C.; Crépon, M. Inertial Oscillations on the Continental Shelf of the Gulf of Lions—Observations and Theory. *J. Phys. Oceanogr.* **1981**, *11*, 639–657. [CrossRef]
3. Park, J.H.; Watts, D.R. Near-inertial oscillations interacting with mesoscale circulation in the southwestern Japan/East Sea. *Geophys. Res. Lett.* **2005**, *32*, 153–174. [CrossRef]
4. Pallàs-Sanz, E.; Candela, J.; Sheinbaum, J.; Ochoa, J.; Jouanno, J. Trapping of the near-inertial wave wakes of two consecutive hurricanes in the Loop Current. *J. Geophys. Res. Ocean.* **2016**, *121*, 7431–7454. [CrossRef]
5. Zhang, Z.; Qiu, B.; Tian, J.; Zhao, W.; Huang, X. Latitude-dependent finescale turbulent shear generations in the Pacific trop-ical-extratropical upper ocean. *Nat. Commun.* **2018**, *9*, 4086. [CrossRef]
6. Whalen, C.B.; MacKinnon, J.A.; Talley, L.D. Large-scale impacts of the mesoscale environment on mixing from wind-driven internal waves. *Nat. Geosci.* **2018**, *11*, 842–847. [CrossRef]
7. Alford, M.H. Redistribution of energy available for ocean mixing by long-range propagation of internal waves. *Nature* **2003**, *423*, 159–162. [CrossRef] [PubMed]
8. Troy, C.D.; Ahmed, S.; Hawley, N.; Goodwell, A. Cross-shelf thermal variability in southern Lake Michigan during the stratified periods. *J. Geophys. Res. Ocean.* **2012**, *117*, C02028. [CrossRef]
9. Jochum, M.; Briegleb, B.P.; Danabasoglu, G.; Large, W.G.; Norton, N.J.; Jayne, S.R.; Alford, M.H.; Bryan, F.O. The Impact of Oceanic Near-Inertial Waves on Climate. *J. Clim.* **2013**, *26*, 2833–2844. [CrossRef]
10. D'Asaro, E.A. The Energy Flux from the Wind to Near-Inertial Motions in the Surface Mixed Layer. *J. Phys. Oceanogr.* **1985**, *15*, 1043–1059. [CrossRef]
11. Yang, B.; Hou, Y.; Hu, P. Observed near-inertial waves in the wake of Typhoon Hagupit in the northern South China Sea. *Chin. J. Oceanol. Limnol.* **2015**, *33*, 1265–1278. [CrossRef]
12. Xie, X.-H.; Shang, X.-D.; Van Haren, H.; Chen, G.-Y.; Zhang, Y.-Z. Observations of parametric subharmonic instability-induced near-inertial waves equatorward of the critical diurnal latitude. *Geophys. Res. Lett.* **2011**, *38*, L05603. [CrossRef]

13. MacKinnon, J.A.; Alford, M.H.; Sun, O.; Pinkel, R.; Zhao, Z.; Klymak, J. Parametric Subharmonic Instability of the Internal Tide at 29° N. *J. Phys. Oceanogr.* **2013**, *43*, 17–28. [CrossRef]
14. Nikurashin, M.; Ferrari, R. Radiation and Dissipation of Internal Waves Generated by Geostrophic Motions Impinging on Small-Scale Topography: Theory. *J. Phys. Oceanogr.* **2010**, *40*, 1055–1074. [CrossRef]
15. Nikurashin, M.; Ferrari, R. Radiation and Dissipation of Internal Waves Generated by Geostrophic Motions Impinging on Small-Scale Topography: Application to the Southern Ocean. *J. Phys. Oceanogr.* **2010**, *40*, 2025–2042. [CrossRef]
16. van Aken, H.M.; Maas, L.R.M.; van Haren, H. Observations of Inertial Wave Events near the Continental Slope off Goban Spur. *J. Phys. Oceanogr.* **2005**, *35*, 1329–1340. [CrossRef]
17. Liang, X.; Thurnherr, A. Eddy-Modulated Internal Waves and Mixing on a Midocean Ridge. *J. Phys. Oceanogr.* **2012**, *42*, 1242–1248. [CrossRef]
18. Hoskins, B.J.; Bretherton, F.P. Atmospheric frontogenesis models: Mathematical formulation and solutions. *J. Atmos. Sci.* **1972**, *29*, 11–37. [CrossRef]
19. Ford, R. Gravity wave radiation from vortex trains in rotating shallow water. *J. Fluid Mech.* **1994**, *281*, 81–118. [CrossRef]
20. Kunze, E. Near-Inertial Wave Propagation in Geostrophic Shear. *J. Phys. Oceanogr.* **1985**, *15*, 544–565. [CrossRef]
21. Kunze, E.; Schmitt, R.W.; Toole, J. The Energy Balance in a Warm-Core Ring's Near-Inertial Critical Layer. *J. Phys. Oceanogr.* **1995**, *25*, 942–957. [CrossRef]
22. Byun, S.-S.; Park, J.J.; Chang, K.-I.; Schmitt, R.W. Observation of near-inertial wave reflections within the thermostad layer of an anticyclonic mesoscale eddy. *Geophys. Res. Lett.* **2010**, *37*, 483–496. [CrossRef]
23. Chen, G.; Xue, H.; Wang, D.; Xie, Q. Observed near-inertial kinetic energy in the northwestern South China Sea. *J. Geophys. Res. Ocean.* **2013**, *118*, 4965–4977. [CrossRef]
24. Guan, S.; Zhao, W.; Huthnance, J.; Tian, J.; Wang, J. Observed upper ocean response to typhoon Megi (2010) in the Northern South China Sea. *J. Geophys. Res. Ocean.* **2014**, *119*, 3134–3157. [CrossRef]
25. Yang, B.; Hu, P.; Hou, Y. Variation and Episodes of Near-Inertial Internal Waves on the Continental Slope of the Southeastern East China Sea. *J. Mar. Sci. Eng.* **2021**, *9*, 916. [CrossRef]
26. Rossby, C.-G. On the Mutual Adjustment of Pressure and Velocity Distributions in Certain Simple Current Systems, II. *J. Mar. Res.* **1938**, *1*, 239–263. [CrossRef]
27. Gill, A.E. On the Behavior of Internal Waves in the Wakes of Storms. *J. Phys. Oceanogr.* **1984**, *14*, 1129–1151. [CrossRef]
28. Qi, H.; De Szoeke, R.A.; Paulson, C.A.; Eriksen, C.C. The Structure of Near-Inertial Waves during Ocean Storms. *J. Phys. Oceanogr.* **1995**, *25*, 2853–2871. [CrossRef]
29. Geisler, J.E. Linear theory of the response of a two layer ocean to a moving hurricane. *Geophys. Fluid Dyn.* **1970**, *1*, 249–272. [CrossRef]
30. Zhang, H.; Chen, D.; Zhou, L.; Liu, X.; Ding, T.; Zhou, B. Upper ocean response to typhoon Kalmaegi (2014). *J. Geophys. Res. Ocean.* **2016**, *121*, 6520–6535. [CrossRef]
31. Firing, E.; Lien, R.-C.; Muller, P. Observations of strong inertial oscillations after the passage of Tropical Cyclone Ofa. *J. Geophys. Res. Ocean.* **1997**, *102*, 3317–3322. [CrossRef]
32. Sanford, T.B.; Price, J.F.; Girton, J.B. Upper-Ocean Response to Hurricane Frances (2004) Observed by Profiling EM-APEX Floats. *J. Phys. Oceanogr.* **2011**, *41*, 1041–1056. [CrossRef]
33. Yang, B.; Hou, Y. Near-inertial waves in the wake of 2011 Typhoon Nesat in the northern South China Sea. *Acta Oceanol. Sin.* **2014**, *33*, 102–111. [CrossRef]
34. Yang, B.; Hou, Y.; Hu, P.; Liu, Z.; Liu, Y. Shallow ocean response to tropical cyclones observed on the continental shelf of the northwestern South China Sea. *J. Geophys. Res. Ocean.* **2015**, *120*, 3817–3836. [CrossRef]
35. Hou, H.; Yu, F.; Nan, F.; Yang, B.; Guan, S.; Zhang, Y. Observation of Near-Inertial Oscillations Induced by Energy Transformation during Typhoons. *Energies* **2019**, *12*, 99. [CrossRef]
36. Jeon, C.; Park, J.-H.; Nakamura, H.; Nishina, A.; Zhu, X.-H.; Kim, D.G.; Min, H.S.; Kang, S.K.; Na, H.; Hirose, N. Poleward-propagating near-inertial waves enabled by the western boundary current. *Sci. Rep.* **2019**, *9*, 9955. [CrossRef]
37. Ma, Y.; Zhang, S.; Qi, Y.; Jing, Z. Upper ocean near-inertial response to the passage of two sequential typhoons in the north-western South China Sea. *Sci. China Earth Sci.* **2019**, *62*, 863–871. [CrossRef]
38. Cao, A.; Guo, Z.; Pan, Y.; Song, J.; He, H.; Li, P. Near-Inertial Waves Induced by Typhoon Megi (2010) in the South China Sea. *J. Mar. Sci. Eng.* **2021**, *9*, 440. [CrossRef]
39. Xu, F.H.; Yuan, Y.; Oey, L.; Lin, Y. Impacts of pre-existing ocean cyclonic circulation on sea surface chlorophyll-a concentrations off northeastern Taiwan following episodic typhoon passages. *J. Geophys. Res. Oceans.* **2017**, *122*, 6482–6497. [CrossRef]
40. He, Y.; Hu, P.; Yang, B.; Yin, Y.; Hou, Y. Volume transport in the East Taiwan Channel in response to different tracks of typhoons as revealed by HYCOM data. *J. Oceanol. Limnol.* **2021**, *40*, 22–36. [CrossRef]
41. Nagai, T.; Durán, G.S.; Otero, D.A.; Mori, Y.; Yoshie, N.; Ohgi, K.; Hasegawa, D.; Nishina, A.; Kobari, T. How the Kuroshio Current Delivers Nutrients to Sunlit Layers on the Continental Shelves with Aid of Near-Inertial Waves and Turbulence. *Geophys. Res. Lett.* **2019**, *46*, 6726–6735. [CrossRef]
42. Whalen, C.B.; De Lavergne, C.; Garabato, A.C.N.; Klymak, J.M.; MacKinnon, J.A.; Sheen, K.L. Internal wave-driven mixing: Governing processes and consequences for climate. *Nat. Rev. Earth Environ.* **2020**, *1*, 606–621. [CrossRef]

43. Ying, M.; Zhang, W.; Yu, H.; Lu, X.; Feng, J.; Fan, Y.; Zhu, Y.; Chen, D. An Overview of the China Meteorological Administration Tropical Cyclone Database. *J. Atmos. Ocean. Technol.* **2014**, *31*, 287–301. [CrossRef]
44. Lu, X.; Yu, H.; Ying, M.; Zhao, B.; Zhang, S.; Lin, L.; Bai, L.; Wan, R. Western North Pacific Tropical Cyclone Database Created by the China Meteorological Administration. *Adv. Atmos. Sci.* **2021**, *38*, 690–699. [CrossRef]
45. He, Y.; Hu, P.; Yin, Y.; Liu, Z.; Liu, Y.; Hou, Y.; Zhang, Y. Vertical Migration of the Along-Slope Counter-Flow and Its Relation with the Kuroshio Intrusion off Northeastern Taiwan. *Remote Sens.* **2019**, *11*, 2624. [CrossRef]
46. Yang, Y.; Wang, D.; Wang, Q.; Zeng, L.; Xing, T.; He, Y.; Shu, Y.; Chen, J.; Wang, Y. Eddy-Induced Transport of Saline Kuroshio Water into the Northern South China Sea. *J. Geophys. Res. Ocean.* **2019**, *124*, 6673–6687. [CrossRef]
47. Silverthorne, K.E.; Toole, J. Seasonal Kinetic Energy Variability of Near-Inertial Motions. *J. Phys. Oceanogr.* **2009**, *39*, 1035–1049. [CrossRef]
48. Leaman, K.D.; Sanford, T.B. Vertical energy propagation of inertial waves: A vector spectral analysis of velocity profiles. *J. Geophys. Res.* **1975**, *80*, 1975–1978. [CrossRef]
49. Oey, L.-Y.; Ezer, T.; Wang, D.-P.; Fan, S.-J.; Yin, X.-Q. Loop Current warming by Hurricane Wilma. *Geophys. Res. Lett.* **2006**, *33*, L08613. [CrossRef]
50. Zhao, Z.; Alford, M.H.; MacKinnon, J.A.; Pinkel, R. Long-Range Propagation of the Semidiurnal Internal Tide from the Hawaiian Ridge. *J. Phys. Oceanogr.* **2010**, *40*, 713–736. [CrossRef]
51. Larsen, L.; Cannon, G.; Choi, B. East China Sea tide currents. *Cont. Shelf Res.* **1985**, *4*, 77–103. [CrossRef]
52. Park, J.-H.; Lie, H.-J.; Guo, B. Observation of Semi-diurnal Internal Tides and Near-inertial Waves at the Shelf Break of the East China Sea. *Ocean Polar Res.* **2011**, *33*, 409–419. [CrossRef]
53. Park, J.J.; Kim, K.; Schmitt, R.W. Global distribution of the decay timescale of mixed layer inertial motions observed by satellite-tracked drifters. *J. Geophys. Res. Earth Surf.* **2009**, *114*, C11010. [CrossRef]
54. Zheng, Q.A.; Lai, R.J.; Huang, N.E.; Pan, J.Y.; Liu, W.T. Observation of ocean current response to 1998 Hurricane Georges in the Gulf of Mexico. *Acta. Oceanol. Sin.* **2006**, *25*, 1–14.
55. Shang, X.; Liu, Q.; Xie, X.; Chen, G.; Chen, R. Characteristics and seasonal variability of internal tides in the southern South China Sea. *Deep Sea Res. Part I Oceanogr. Res. Pap.* **2015**, *98*, 43–52. [CrossRef]
56. Wagner, G.L.; Young, W.R. A three-component model for the coupled evolution of near-inertial waves, quasi-geostrophic flow and the near-inertial second harmonic. *J. Fluid Mech.* **2016**, *802*, 806–837. [CrossRef]
57. Le Boyer, A.; Alford, M.H.; Pinkel, R.; Hennon, T.D.; Yang, Y.J.; Ko, D.; Nash, J. Frequency Shift of Near-Inertial Waves in the South China Sea. *J. Phys. Oceanogr.* **2020**, *50*, 1121–1135. [CrossRef]
58. Alford, M.H.; Gregg, M.C. Near-inertial mixing: Modulation of shear, strain and microstructure at low latitude. *J. Geophys. Res. Earth Surf.* **2001**, *106*, 16947–16968. [CrossRef]
59. Anderson, D.L.T.; Gill, A.E. Beta dispersion of inertial waves. *J. Geophys. Res. Earth Surf.* **1979**, *84*, 1836–1842. [CrossRef]
60. Nencioli, F.; Dong, C.M.; Dickey, T.; Washburn, L.; Mcwilliams, J.C. A vector geometry-based detection algorithm and its application to a high-resolution numerical model product and high-frequency radar surface velocities in the southern California Bright. *J. Atmos. Ocean Technol.* **2010**, *27*, 564–579. [CrossRef]
61. Pollard, R.; Millard, R. Comparison between observed and simulated wind-generated inertial oscillations. *Deep Sea Res. Oceanogr. Abstr.* **1970**, *17*, 813–821. [CrossRef]
62. Alford, M.H. Internal swell generation: The spatial distribution of energy flux from the wind to mixed layer near-inertial motions. *J. Phys. Oceanogr.* **2001**, *31*, 2359–2368. [CrossRef]
63. Sprintall, J.; Tomczak, M. Evidence of the barrier layer in the surface layer of the tropics. *J. Geophys. Res. Ocean.* **1992**, *97*, 7305–7316. [CrossRef]
64. Dohan, K.; Davis, R.E. Mixing in the Transition Layer during Two Storm Events. *J. Phys. Oceanogr.* **2011**, *41*, 42–66. [CrossRef]
65. Johnston, T.M.S.; Chaudhuri, D.; Mathur, M.; Rudnick, D.; Sengupta, D.; Simmons, H.; Tandon, A.; Venkatesan, R. Decay Mechanisms of Near-Inertial Mixed Layer Oscillations in the Bay of Bengal. *Oceanography* **2016**, *29*, 180–191. [CrossRef]
66. D’Asaro, E.A. A collection of papers on the ocean storms experiment. *J. Phys. Oceanogr.* **1995**, *25*, 2817–2818.
67. Niwa, Y.; Hibiya, T. Three-dimensional numerical simulation of M2 internal tides in the East China Sea. *J. Geophys. Res.* **2004**, *109*, C04027. [CrossRef]
68. Niwa, Y.; Hibiya, T. Generation of baroclinic tide energy in a global three-dimensional numerical model with different spatial grid resolutions. *Ocean Model.* **2014**, *80*, 59–73. [CrossRef]
69. Tian, J.; Zhou, L.; Zhang, X. Latitudinal Distribution of Mixing Rate Caused by the M2 Internal Tide. *J. Phys. Oceanogr.* **2006**, *36*, 35–42. [CrossRef]
70. Fer, I. Near-Inertial Mixing in the Central Arctic Ocean. *J. Phys. Oceanogr.* **2014**, *44*, 2031–2049. [CrossRef]
71. Müller, P.; Holloway, G.; Henyey, F.; Pomphrey, N. Nonlinear interactions among internal gravity waves. *Rev. Geophys.* **1986**, *24*, 493–536. [CrossRef]
72. Kim, Y.C.; Powers, E.J. Digital Bispectral Analysis and Its Applications to Nonlinear Wave Interactions. *IEEE Trans. Plasma Sci.* **1979**, *7*, 120–131. [CrossRef]
73. Mccomas, C.H.; Briscoe, M.G. Bispectra of internal waves. *J. Fluid Mech.* **1980**, *97*, 205–213. [CrossRef]
74. Carter, G.S.; Gregg, M.C. Persistent Near-Diurnal Internal Waves Observed above a Site of M2 Barotropic-to-Baroclinic Conversion. *J. Phys. Oceanogr.* **2006**, *36*, 1136–1147. [CrossRef]

75. Cao, A.; Guo, Z.; Song, J.; Lv, X.; He, H.; Fan, W. Near-Inertial Waves and Their Underlying Mechanisms Based on the South China Sea Internal Wave Experiment (2010–2011). *J. Geophys. Res. Ocean.* **2018**, *123*, 5026–5040. [CrossRef]
76. Yang, W.; Wei, H.; Zhao, L. Parametric Subharmonic Instability of the Semidiurnal Internal Tides at the East China Sea Shelf Slope. *J. Phys. Oceanogr.* **2020**, *50*, 907–920. [CrossRef]